Article

Cell

Nuclear Import Receptor Inhibits Phase Separation of FUS through Binding to Multiple Sites

Graphical Abstract

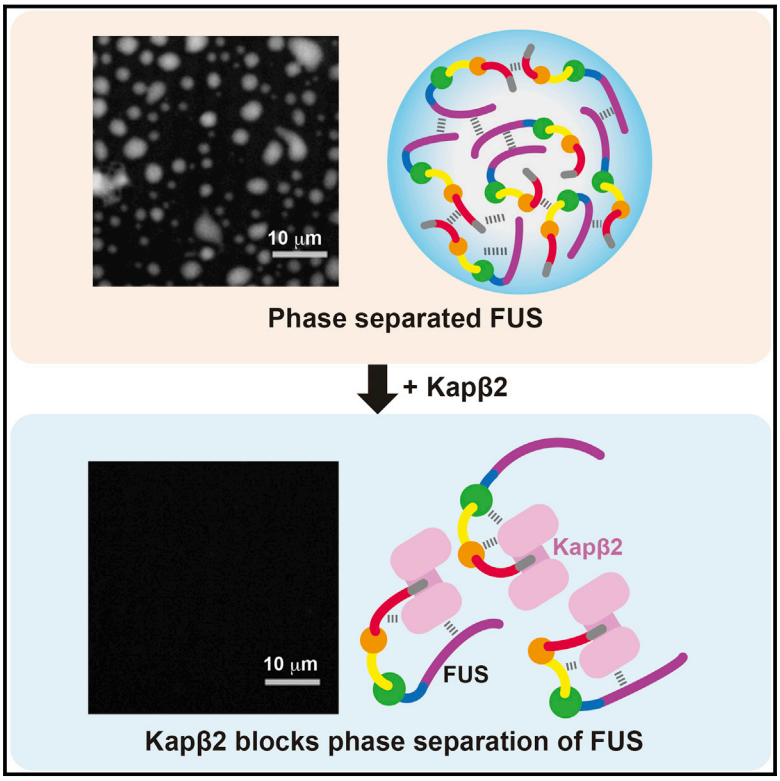

Authors

Takuya Yoshizawa, Rustam Ali, Jenny Jiou, ..., Nicolas L. Fawzi, Michael K. Rosen, Yuh Min Chook

Correspondence

michael.rosen@utsouthwestern.edu (M.K.R.), yuhmin.chook@utsouthwestern.edu (Y.M.C.)

In Brief

Distributed, energetically weak interactions between a karyopherin and the FUS nuclear localization signal disrupt FUS phase separation.

Highlights

- Karyopherin-β2 inhibits liquid-liquid phase separation of FUS
- Kapβ2 binds tightly to the PY-NLS and weakly to multiple regions across FUS
- Many of these regions also promote FUS phase separation
- Kapβ2-FUS interactions compete with FUS-FUS interactions to disrupt phase separation

Yoshizawa et al., 2018, Cell *173*, 693–705
April 19, 2018
https://doi.org/10.1016/j.cell.2018.03.003

CellPress

Article

Cell

Nuclear Import Receptor Inhibits Phase Separation of FUS through Binding to Multiple Sites

Takuya Yoshizawa,[1,7] Rustam Ali,[2,7] Jenny Jiou,[1] Ho Yee Joyce Fung,[1] Kathleen A. Burke,[3] Seung Joong Kim,[4] Yuan Lin,[2,5] William B. Peeples,[2,5] Daniel Saltzberg,[4] Michael Soniat,[1] Jordan M. Baumhardt,[1] Rudolf Oldenbourg,[6] Andrej Sali,[4] Nicolas L. Fawzi,[3] Michael K. Rosen,[2,5,*] and Yuh Min Chook[1,5,8,*]

[1]Department of Pharmacology, University of Texas Southwestern Medical Center, Dallas, TX 75390, USA
[2]Department of Biophysics and Howard Hughes Medical Institute, University of Texas Southwestern Medical Center, Dallas, TX 75390, USA
[3]Department of Molecular Pharmacology, Physiology and Biotechnology, Brown University, Providence, RI 02912, USA
[4]Department of Bioengineering and Therapeutic Sciences, Department of Pharmaceutical Chemistry, California Institute for Quantitative Biosciences, University of California, San Francisco, San Francisco, CA 94158, USA
[5]Howard Hughes Medical Institute (HHMI) Summer Institute, Marine Biological Laboratory, Woods Hole, MA 02543, USA
[6]Marine Biological Laboratories, 7 MBL Street, Woods Hole, MA 02543, USA
[7]These authors contributed equally
[8]Lead Contact
*Correspondence: michael.rosen@utsouthwestern.edu (M.K.R.), yuhmin.chook@utsouthwestern.edu (Y.M.C.)
https://doi.org/10.1016/j.cell.2018.03.003

SUMMARY

Liquid-liquid phase separation (LLPS) is believed to underlie formation of biomolecular condensates, cellular compartments that concentrate macromolecules without surrounding membranes. Physical mechanisms that control condensate formation/dissolution are poorly understood. The RNA-binding protein fused in sarcoma (FUS) undergoes LLPS *in vitro* and associates with condensates in cells. We show that the importin karyopherin-β2/transportin-1 inhibits LLPS of FUS. This activity depends on tight binding of karyopherin-β2 to the C-terminal proline-tyrosine nuclear localization signal (PY-NLS) of FUS. *Nuclear magnetic resonance* (NMR) analyses reveal weak interactions of karyopherin-β2 with sequence elements and structural domains distributed throughout the entirety of FUS. Biochemical analyses demonstrate that most of these same regions also contribute to LLPS of FUS. The data lead to a model where high-affinity binding of karyopherin-β2 to the FUS PY-NLS tethers the proteins together, allowing multiple, distributed weak intermolecular contacts to disrupt FUS self-association, blocking LLPS. Karyopherin-β2 may act analogously to control condensates in diverse cellular contexts.

INTRODUCTION

The RNA-binding protein fused in sarcoma (FUS) plays roles in transcription, RNA processing, and DNA repair (Ederle and Dormann, 2017). FUS is localized primarily to the nucleus but is also found in cytoplasmic ribonucleoprotein (RNP) granules (Crozat et al., 1993; Ryu et al., 2014). Heat shock and DNA damage promote localization of the protein to cytoplasmic and nuclear puncta (Patel et al., 2015). FUS is involved in diverse diseases including cancer and the neurodegenerative diseases amyotrophic lateral sclerosis (ALS) and frontotemporal lobar degeneration (FTLD) (Harrison and Shorter, 2017; Schwartz et al., 2015). In ALS, FUS is often mutated in its proline-tyrosine nuclear localization sequence (PY-NLS). These alterations decrease affinity for the nuclear import factor karyopherin-β2 (Kapβ2; also known as transportin-1) leading to aberrant cytoplasmic localization and enrichment in RNP granules (Dormann and Haass, 2011; Zhang and Chook, 2012). Proper compartmentalization of FUS is important in maintaining cellular homeostasis, as the degree of FUS mislocalization correlates with ALS onset and severity (Dormann and Haass, 2011).

FUS is composed of multiple structural and functional elements. It has an N-terminal disordered region with low amino acid sequence complexity that is enriched in Gly, Ser, Tyr, and Gln residues (low amino acid sequence complexity [LC] region), followed by a segment with Arg-Gly-Gly motifs (RGG1), a folded RNA recognition motif (RRM) domain, two additional RGG regions (RGG2 and RGG3) flanking a zinc-finger (ZnF) domain, and a C-terminal 26-residue PY-NLS (Figure 1A) (Ederle and Dormann, 2017). FUS is highly prone to self-association, a process that can lead to different material states including phase-separated liquids, amyloid fiber containing hydrogels, and aggregated solids (Burke et al., 2015; Kato et al., 2012; Murakami et al., 2015; Sun et al., 2011). The LC region undergoes liquid-liquid phase separation (LLPS) at high concentrations, through weak and transient homotypic interactions (Burke et al., 2015; Lin et al., 2015). Full-length FUS also undergoes LLPS, but at much lower concentrations, consistent with previous reports that the RGG regions can contribute to self-association of the protein (Patel et al., 2015; Sun et al., 2011). RNA enhances these processes (Burke et al., 2015; Schwartz et al., 2013). Phase separation of FUS and other disordered proteins is driven by a variety of interaction types including charge-charge, cation-π, π-π stacking,

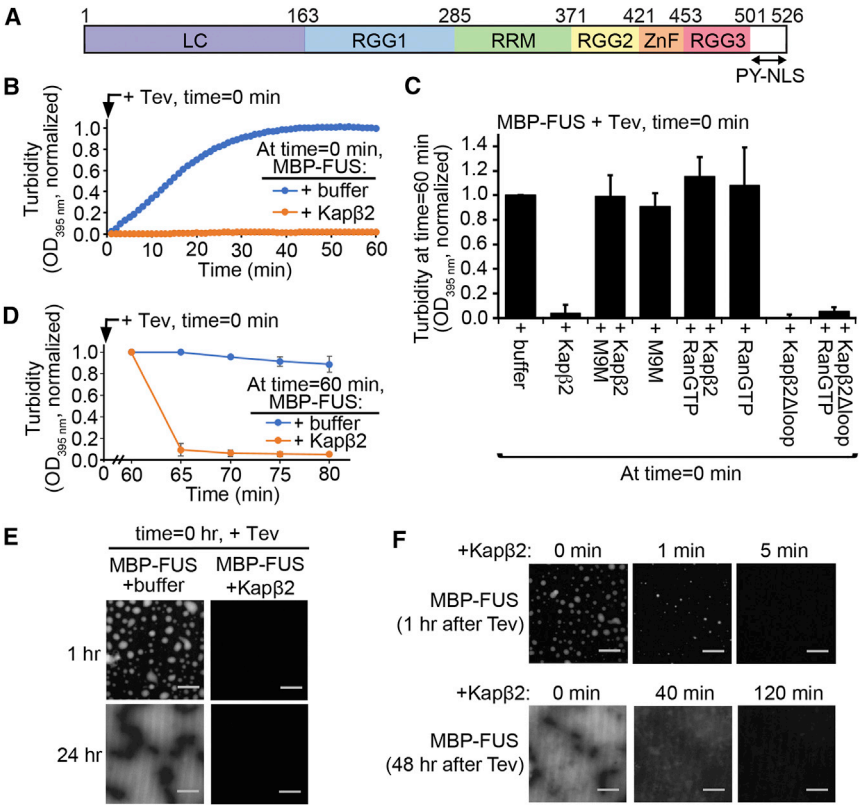

Figure 1. Kapβ2 Inhibits FUS Turbidity and Phase Separation in a PY-NLS- and RanGTP-Dependent Manner

(A) Domain organization of FUS.

(B) Turbidity of 8 μM MBP-FUS ± 8 μM Kapβ2, measured for 60 min at room temperature after addition of Tev protease to remove MBP from MBP-FUS. OD_{395nm} normalized to measurements of MBP-FUS + buffer + Tev at time = 60 min.

(C) Turbidity of 8 μM MBP-FUS in the presence of buffer, 8 μM Kapβ2 ± RanGTP or inhibitor M9M, or Kapβ2Δloop ± RanGTP (60 min after Tev). OD_{395nm} normalized to measurements of MBP-FUS + buffer + Tev at time = 60 min. Mean of 3 technical replicates, ±SD.

(D) Either 8 μM Kapβ2 or buffer was added at time = 60 min to turbid FUS (8 μM MBP-FUS pre-treated with Tev for 60 min) and OD_{395nm} measured for the next 20 min. OD_{395nm} normalized to measurements of MBP-FUS + buffer + Tev at time = 60 min. Mean of 3 technical replicates, ±SD.

(E) Mixtures containing 5 μM MBP-FUS, 0.5 μM MBP-FUS-$SNAP^{SNAP\text{-}Surface\ 649}$, and either buffer or 10 μM Kapβ2 were treated with Tev and imaged 1 hr later. Video S1 also shows FUS droplets at time = 1 hr.

(F) Mixtures of 5 μM MBP-FUS and 0.5 μM MBP-FUS-$SNAP^{SNAP\text{-}Surface\ 649}$ were treated with Tev for 1 hr prior to addition of 10 μM of Kapβ2, which cleared FUS droplets in <5 min (see also Video S2). Kapβ2 added to phase-separated FUS 48 hr after Tev treatment cleared most of the phase-separated material in 120 min (Video S3 also shows the first 30 min after Kapβ2 addition). Images in (E) and (F) were obtained with spinning disk confocal microscopy (561 nm laser illumination; 60× 1.4 n.a. oil immersion objective lenses), and 20-μm length scale bars are shown.

See also Figure S1.

and hydrogen bonds, involving side chains and backbone (Banani et al., 2017; Brangwynne et al., 2015). Over time, phase-separated FUS droplets mature to more solid hydrogels that contain amyloid-like fibers (Burke et al., 2015; Kato et al., 2012; Lin et al., 2015; Murakami et al., 2015; Patel et al., 2015). Disease-causing mutations accelerate maturation of FUS droplets *in vitro* (Murakami et al., 2015; Patel et al., 2015). A recent solid state *nuclear magnetic resonance* (NMR) analysis of fibers formed by the FUS LC region revealed a β strand-containing structured core spanning residues 39–95, whose formation also appears to contribute to LLPS (Murray et al., 2017). Similar LLPS and maturation behaviors have been observed for other RNA binding proteins containing disordered or LC regions (Lin et al., 2015; Molliex et al., 2015; Xiang et al., 2015). The progression from phase-separated liquid to a more static solid is likely controlled in cells to produce structures of different material properties, according to specific cellular needs. However, the biological factors that can control self-association, LLPS, and fiber formation of FUS are not known.

The FUS PY-NLS and its ALS-associated mutations seem to play no direct role in FUS self-association (Ju et al., 2011; Sun et al., 2011). However, FUS PY-NLS binding to Kapβ2 controls nuclear-cytoplasmic localization of FUS and cytoplasmic concentrations of FUS likely controls self-association and disease onset (Dormann and Haass, 2011). Kapβ2 is also the only high-affinity binding partner of FUS that has been characterized to date (Zhang and Chook, 2012). Although it is well established that Kapβ2 imports FUS into the nucleus, it is not known if Kapβ2 binding directly affects FUS self-association and/or its ability to undergo LLPS.

Here, we show that Kapβ2 inhibits LLPS of FUS, in a manner dependent on interactions with the FUS PY-NLS. The importin-α•importin-β (Impα/β) heterodimer and the yeast Kap121, can also inhibit FUS LLPS when the FUS PY-NLS is replaced with the appropriate cognate NLSs. Thus, importins may generally be able to control LLPS of self-associating RNA-binding proteins through high-affinity binding to their NLSs. NMR analyses reveal multiple weak interactions of Kapβ2 with both folded and disordered regions across FUS. Deletion or mutation of some of these elements (LC, RGG2, and RGG3) also decreases phase separation of FUS. Together, the data suggest that high-affinity interactions between Kapβ2 and the PY-NLS of FUS anchor the two proteins together, facilitating multiple weak interactions with FUS regions that mediate self-association, thus blocking phase separation. These effects may enable Kapβ2, and perhaps other importin family members, to control the stability and dynamics of RNA-containing biomolecular condensates.

RESULTS

Kapβ2 Prevents and Reverses Turbidity of FUS Solutions

Purified bacterially expressed maltose binding protein-FUS fusion protein (MBP-FUS) is soluble and monomeric by gel filtration chromatography. The protein is polydisperse in dynamic light scattering experiments, however, suggesting the presence of minor high molecular weight oligomers (Figure S1A). The PY-NLS of FUS binds the 100 kDa Kapβ2 with dissociation constant (K_D) of 70 nM (Figure S1B). MBP-FUS also binds Kapβ2 stably, but the affinity is difficult to quantify because of the polydispersity of MBP-FUS. An approximate K_D determined by isothermal titration calorimetry (ITC) is 160 nM (Figure S1B). Addition of Kapβ2 to MBP-FUS drastically reduced polydispersity. The majority of MBP-FUS•Kapβ2 behaves as a single species, most likely the heterodimer (Figure S1C), suggesting that Kapβ2 can disrupt self-association of FUS.

Removal of MBP from MBP-FUS with the Tev protease causes FUS to self-associate, producing a turbid solution (Figures 1B, S1D, and S1E). Addition of equimolar Kapβ2 prior to Tev cleavage prevents turbidity, consistent with formation of soluble Kapβ2•FUS heterodimer (Figures 1B, 1C, and S1C). The ability of Kapβ2 to prevent turbidity is abolished by the M9M peptide inhibitor or the Ran GTPase (Figure 1C), which both displace cargos from Kapβ2 (Cansizoglu et al., 2007; Chook and Blobel, 1999). Kapβ2Δloop mutant, which can bind both RanGTP and PY-NLS simultaneously (Chook et al., 2002), retains the ability to block turbidity even in the presence of RanGTP (Figure 1C). Together, these data show that the ability of Kapβ2 to inhibit turbidity of FUS solutions is dependent on binding to the C-terminal PY-NLS of FUS, the same interaction that mediates nuclear import of FUS. Analogous behavior is also observed when Kapβ2 is added 60 min after turbidity is induced by Tev addition (Figures 1D and S1F). Thus, Kapβ2 can both inhibit and reverse turbidity caused by FUS self-association.

Kapβ2 Inhibits Liquid-Liquid Phase Separation of FUS

We examined turbid solutions of fluorescently labeled FUS (5 μM MBP-FUS doped with 0.5 μM fluorescent MBP-FUS-SNAP$^{\text{SNAP-Surface 649}}$) in the presence of Kapβ2 and its regulators using spinning disc confocal microscopy (Figures 1E, 1F, and S1G). As previously reported (Burke et al., 2015; Monahan et al., 2017; Patel et al., 2015), after removal of MBP, FUS concentrates into phase-separated liquid droplets. When analyzed by polarized light microscopy, the interiors of FUS droplets show no molecular order on 350 nm length scale, consistent with them being a homogeneous liquid phase (Figure S1H). FUS droplets fuse with each other and by 24 hr accumulate into large mats of phase-separated liquid (Figures 1E and S1G; Video S1). As in the turbidity assays above, Kapβ2 can block phase separation of FUS and this activity is inhibited by both RanGTP and the M9M inhibitor (Figures 1E and S1G). Further, Kapβ2 can disrupt phase-separated FUS droplets when added at either 1 hr or 48 hr after Tev addition, although clearance of droplets takes longer in the latter case (Figure 1F; Videos S2 and S3).

Other Importins Can Also Prevent FUS LLPS If Their Cognate NLS Is Present

We next examined whether two other importins with distinct cargo recognition sequences, the Impα/β heterodimer and the *S. cerevisiae* importin Kap121, can also bind FUS and block its LLPS. Cognate cargo recognition sequences for Impα/β and Kap121 are the classical NLS (cNLS) and the isoleucine-lysine NLS (IK-NLS), respectively (Soniat and Chook, 2016). Initially we examined interactions of immobilized GST-Kapβ2, GST-Impα•Impβ, and GST-Kap121 with MBP-FUS in pull-down binding and turbidity assays. We found that GST-Kapβ2 binds well to MBP-FUS but GST-Impα•Impβ does not (Figure S2A), consistent with Impα/β not affecting FUS turbidity (Figure 2A). In contrast, GST-Kap121 binds weakly to MBP-FUS (MBP-FUS band sub-stoichiometric to GST-Kap121 band; Figure S2A), and Kap121 partially prevents FUS turbidity (Figure 2A). When bound to IK-NLS, Kap121 no longer affects FUS turbidity suggesting that Kap121 likely uses its cargo-binding site to bind FUS weakly (Figure 2A).

To learn whether the lack of activity of Impα/β could be due simply to low affinity for FUS, we replaced the PY-NLS in FUS (residues 501–526) with a high-affinity cNLS to give FUS(cNLS). Pull-down binding assays showed that MBP-FUS(cNLS) binds both Impα alone and Impα/β, consistent with direct binding to Impα, as observed for all known Impα/β cargos (Figure S2A). In turbidity assays, Impα alone had no effect on FUS(cNLS) turbidity, but Impα/β blocked turbidity in a RanGTP-sensitive manner (Figure 2B). We also replaced the PY-NLS of FUS with an IK-NLS to give FUS(IK-NLS) (Kobayashi and Matsuura, 2013). Analogous to the results above, LLPS of this chimera is strongly inhibited by Kap121 in a RanGTP-sensitive manner (Figure 2C). In summary, when FUS has an appropriate high-affinity recognition signal, an importin family member that is distinct from Kapβ2 can block its phase-separation. This inhibition requires a β-importin family member as Impα alone has no effect.

Kapβ2 Is Unlikely to Act Non-specifically to Disrupt LLPS

Previous studies reported that FUS PY-NLS does not participate directly in FUS self-association (Ju et al., 2011; Sun et al., 2011). It is therefore unclear how Kapβ2 binding to this element could block LLPS by FUS. One limiting possibility is that simply tethering any large molecule to the C terminus of FUS may act non-specifically to alter the balance between FUS-FUS and FUS-solvent interactions, disfavoring the former and thus inhibiting LLPS. Alternatively, Kapβ2 may be acting specifically, through binding competitively to regions of FUS that mediate self-association.

To examine the former possibility, we replaced the FUS PY-NLS with a high-affinity nuclear export signal (NES) to generate a FUS(NES) chimera (Ohshima et al., 1999). In contrast to the FUS(cNLS) and FUS(IK-NLS) chimeras, phase separation of FUS(NES) was not inhibited by its cognate Kapβ protein, the 127 kDa Exportin CRM1/XPO1 (Figure 2D) even though the two proteins bind each other tightly (Figure S2A). Similarly as described above, the 60 kDa Impα does not disrupt LLPS of FUS(cNLS) (Figures 2B and S2A). Thus, merely tethering large proteins to the FUS C terminus is insufficient to inhibit LLPS.

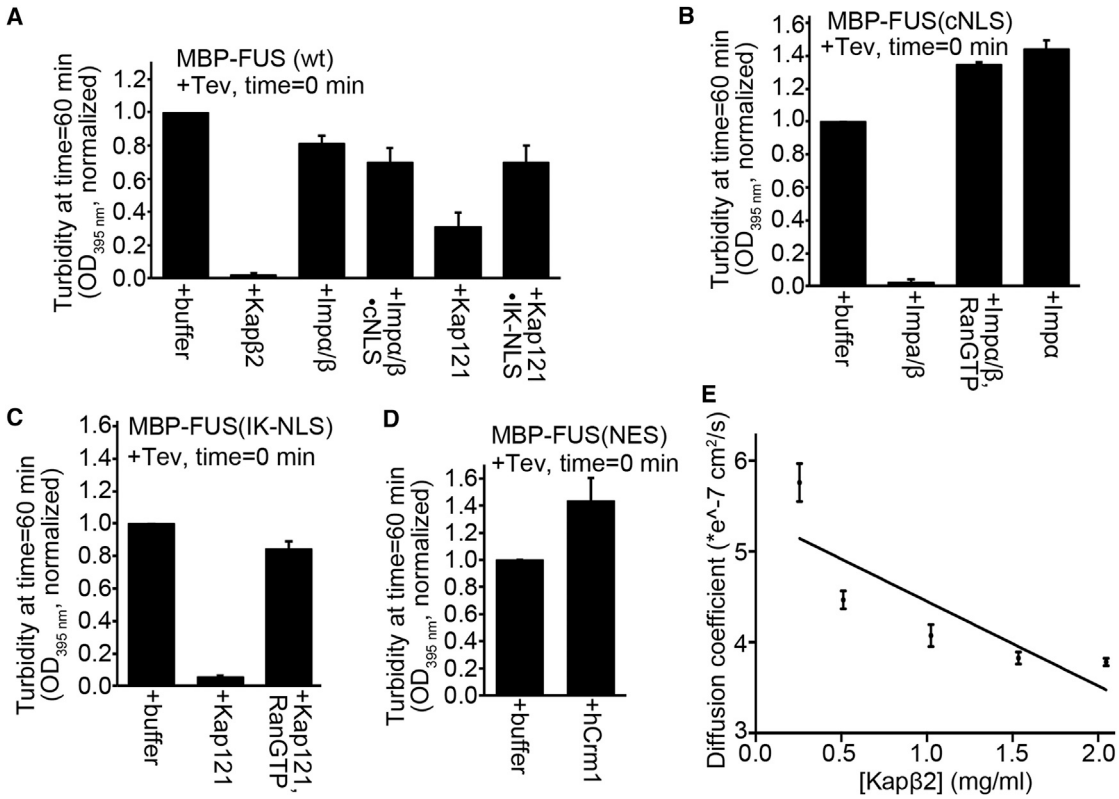

Figure 2. Impα/β and Kap121 Inhibit FUS Phase Separation When Their NLS Is Introduced into FUS, but Kapβ2 Does Not Act Non-specifically to Inhibit FUS Phase Separation

(A) Turbidity of wild-type FUS in the presence of buffer, Kapβ2, Impα/β, cNLS-bound Impα/β, Kap121, or IK-NLS-bound Kap121.

(B) Turbidity of FUS(cNLS) chimera (FUS PY-NLS replaced with the SV40 T antigen cNLS) in the presence of buffer, Impα/β, Impα/β•RanGTP, or Impα.

(C) Turbidity of FUS(IK-NLS) chimera (PY-NLS replaced with IK-NLS from Pho4) in the presence of buffer, Kap121, or Kap121•RanGTP.

(D) Turbidity of FUS(NES) chimera (PY-NLS replaced with the NES from the NS2 protein of MVM virus) in the presence of buffer or CRM1. 8 μM proteins were used in (A–D), and OD_{395nm} were normalized to those of MBP-FUS + buffer + Tev at time = 60 min.

(E) Diffusion coefficients of Kapβ2 were measured at different concentrations by dynamic light scattering. Error bars represent SD from 3 technical replicates. See also Figure S2 and Table S1.

We recently showed that tethering self-attractive proteins to a phase-separating system increases the drive to phase separate, and tethering self-repulsive proteins has an opposite effect (Lin et al., 2017). To investigate whether Kapβ2 has attractive or repulsive self-interactions, we measured its diffusion interaction parameter, κ_D; positive κ_D suggests net repulsive interactions and negative κ_D indicates net attractive interactions (Connolly et al., 2012). As shown in Figure 2E, Kapβ2 has $\kappa_D = -173$ mL/g, indicating attractive self-interactions. Thus, the protein is unlikely to act non-specifically to generate repulsion between FUS molecules.

Kapβ2 Interacts Weakly and Non-uniformly with Residues in FUS LC

FUS is believed to phase-separate due to weak homotypic interactions involving the LC region and C-terminal elements (Burke et al., 2015; Monahan et al., 2017; Patel et al., 2015). Kapβ2 could block phase separation by competitively binding these elements, which are outside of the PY-NLS. The affinities of Kapβ2 for full-length FUS and the FUS PY-NLS are similar ($K_D \sim 160$ nM versus ~70 nM) suggesting that such additional interactions are likely weak (Figure S1B). The lack of stable Kapβ2•FUS contacts outside the PY-NLS is consistent with observations that only the PY-NLS is observed in crystal structures of Kapβ2 bound to FUS (full-length), FUS(371-526), and FUS(456-526) (crystallographic statistics in Table S1; ITC analysis, structures, and electron density maps shown in Figures S2B–S2H).

We used NMR spectroscopy to identify regions of FUS outside its C-terminal PY-NLS that contact Kapβ2 (Figures 3A, 3B, 4A–4E, and 5A–5E). β-importin proteins make many weak and highly dynamic interactions with phenylalanine-glycine (FG) repeats in various nucleoporins to traverse the nuclear pore complex (Hough et al., 2015; Milles et al., 2015). The FUS LC (residues 1–163) contains 24 motifs with the sequence [S/G]Y[S/G] (Figures 3A, 3B, S3A, and S3B), potentially analogous to the FG repeats in the nuclear pore complex. Thus, we initially analyzed $^{1}H/^{15}N$ HSQC spectra of ^{15}N-FUS LC in the absence and presence of Kapβ2 to identify such contacts (Figures 3A and S3A). At conditions where FUS LC is not phase-separated (75 μM, 10°C), many resonances progressively shift and

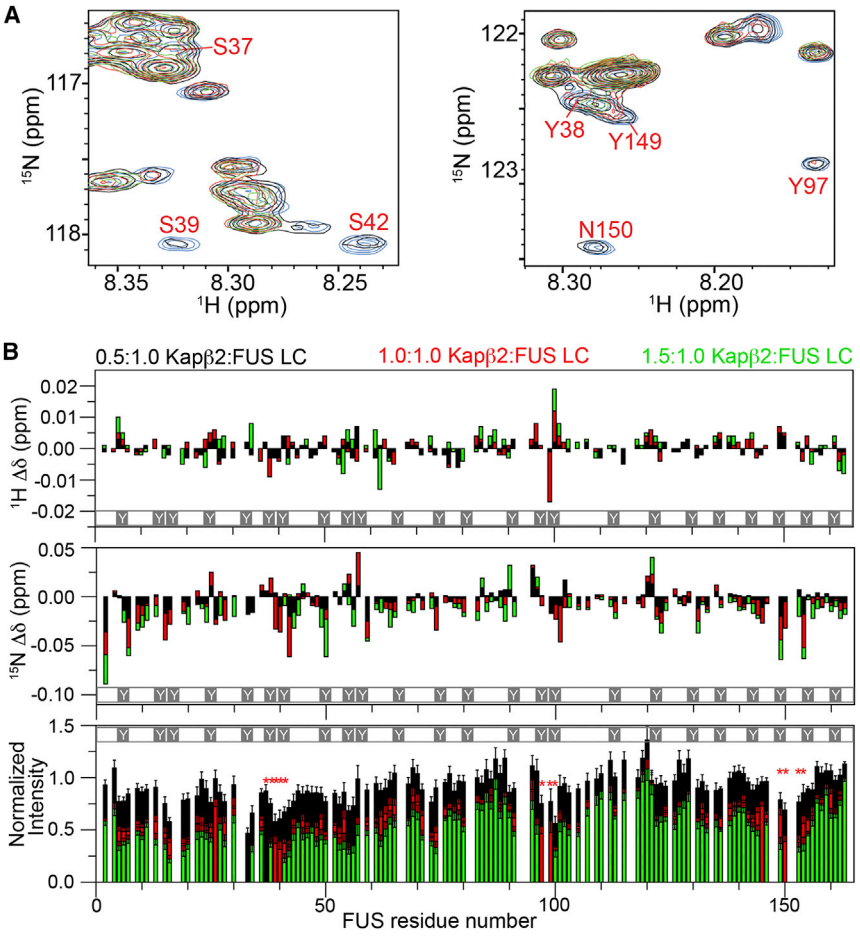

Figure 3. Kapβ2 Interacts Weakly and Non-uniformly with Residues in FUS LC

(A) Overlay of 2D ^{1}H/^{15}N spectra of 75 μM ^{15}N-FUS LC alone (blue) or with increasing concentrations of Kapβ2: 37.5 μM (0.5:1, black), 75 μM (1:1, red), 112.5 μM (1.5:1, green), showing three of the FUS LC regions (residues 37–41, 97–100, 149–154) most affected by Kapβ2 resulting in chemical shifts and intensity attenuations.

(B) Titrations at 10°C of 75 μM FUS LC with increasing concentrations of Kapβ2 compared to FUS LC alone. NMR chemical shift deviations, ^{1}H (top) and ^{15}N (middle), and resonance intensity attenuation (bottom) are plotted. Increasing extent of chemical shift differences of ^{1}H and ^{15}N resonance position, as well as resonance intensity attenuation, support Kapβ2 binding weakly to across the entire FUS LC domain. Resonance intensity attenuation and chemical shifts are non-uniformly distributed as segments ^{37}SYSGY^{41}, ^{97}YPGY^{100}, and ^{149}YSPPSG^{154} (white Ys mark the 24 tyrosines in FUS LC) show the largest perturbations in amide resonance intensity (red asterisks, bottom panel) in the presence of Kapβ2. These segments also show large ^{15}N and/or ^{1}H chemical shift deviations.

Error bars in (B) represent errors propagated from the measurement of noise in the NMR spectra. See also Figure S3.

decrease in intensity as Kapβ2 is increased from 0 to 112.5 μM (Figure 3B; chemical shift assignments from Burke et al. [2015]). These behaviors are consistent with weak binding that is not saturated at these conditions. The attenuation/shifting of FUS LC resonances is distributed non-uniformly across the protein. The largest perturbations are observed for resonances from the segments ^{37}SYSGY^{41}, ^{97}YPGY^{100}, and ^{149}YSPPSG^{154}, suggesting relatively stronger binding to these elements (Figures 3B and S3B). The ^{37}SYSGY^{41} is part of the β strand-containing structured core observed in solid state NMR analysis of LC fibers (Murray et al., 2017), suggesting that disruption of the core may contribute to the effects of Kapβ2. Amide resonances change similarly upon addition of Kapβ2 alone or Kapβ2•PY-NLS, indicating contacts outside the PY-NLS binding site of the karyopherin (Figure S3B).

Kapβ2 Interacts Weakly with Folded and Disordered Regions within FUS(164–500)

Beyond the LC region, C-terminal elements also contribute to LLPS of FUS (Burke et al., 2015; Monahan et al., 2017). Thus, we next examined interactions of FUS(164-500) with Kapβ2. Because of the complex nature of this fragment, containing two folded domains surrounded by three intrinsically disordered elements, we used NMR cross saturation transfer experiments to look for regions that directly contact Kapβ2. In these experiments, ^{15}N/^{2}H-labeled FUS(164-500) (protonated at amide positions, deuterated at all aliphatic sites) is mixed with fully protonated Kapβ2. Irradiation of such samples in the aliphatic region of the spectrum saturates resonances of Kapβ2 and this saturation is transferred to amides of FUS that are in direct contact with the karyopherin. Saturation is manifest as decreases in intensity of selected amide resonances in FUS, which are observed in HSQC-type ^{1}H/^{15}N correlation spectra. The experiment can be complicated by the dynamics of the interactions, such that decreases at bona fide interfaces may not be observed if the bound populations are low or interaction kinetics are in the wrong rate regime (Jayalakshmi and Krishna, 2002; Ueda et al., 2014). The data can be particularly complicated in interactions of disordered proteins, where different parts of the chain may contact a partner with different local dynamics.

Addition of Kapβ2 to ^{15}N-FUS(164-526) harboring the PY-NLS causes severe line-broadening of most resonances in ^{1}H/^{15}N HSQC spectra, including all of those representing the folded domains and much of the disordered regions thus precluding analysis (Figure S4A). This broadening probably occurs because of the large size of the FUS•Kapβ2 complex (~160 kDa) and slow exchange between the bound and free states arising from the high-affinity interaction. Thus, to weaken the interactions and identify direct Kapβ2 contact sites, we recorded spectra on ^{15}N/^{2}H-FUS(164-500) lacking the PY-NLS, in the presence of Kapβ2 bound to the pM affinity M9M peptide inhibitor (to exclude artifactual contacts to the PY-NLS binding

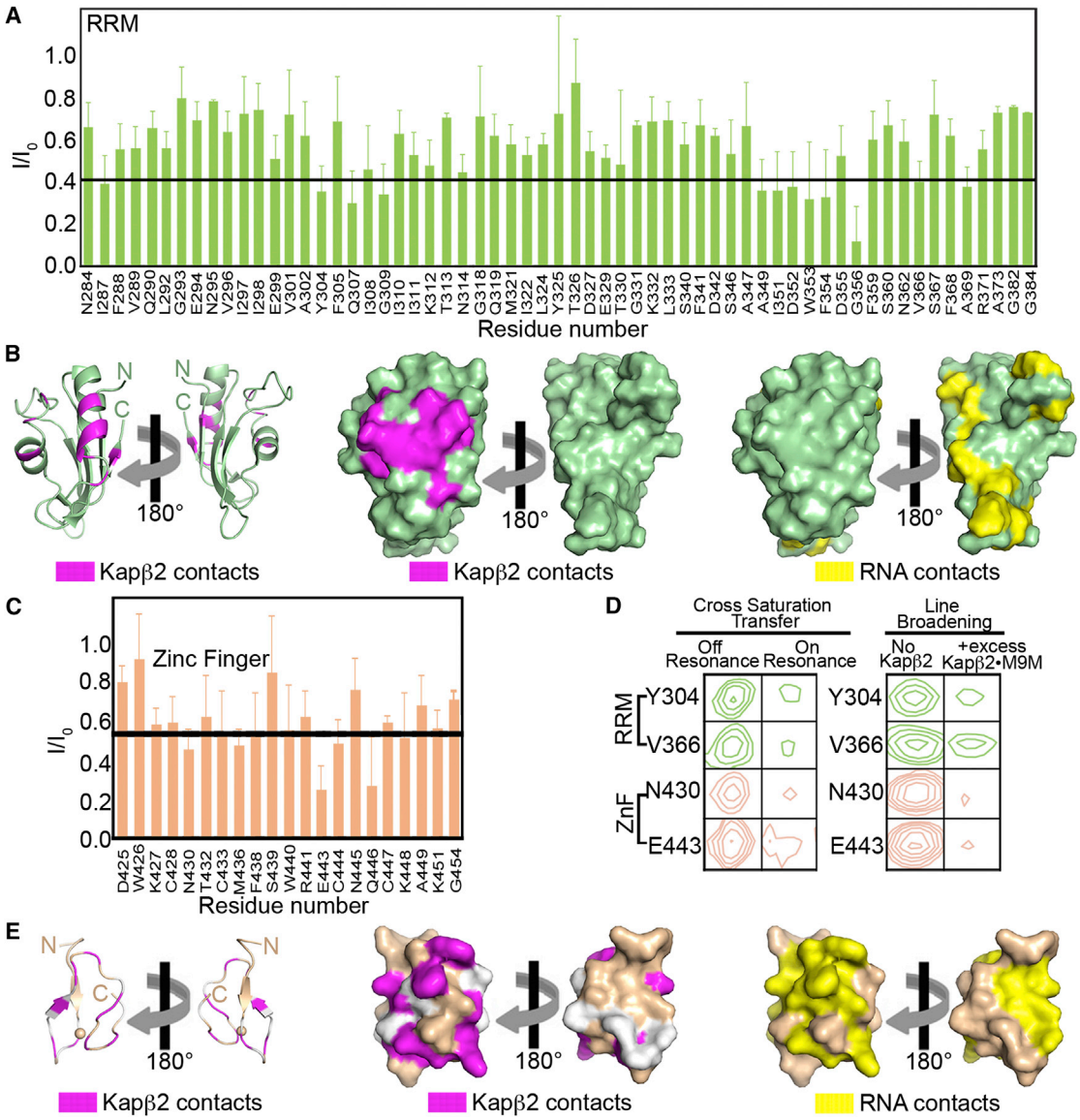

Figure 4. Kapβ2 Interacts Weakly with the Folded RRM and ZnF Domains within FUS(164-500)

(A) Attenuations in intensity (I/I_0) of assigned RRM domain non-proline resonances in FUS(164-500) in the cross saturation transfer experiment. Deuterated ^{15}N-FUS(164-500) was cross saturated from protonated Kapβ2-M9M (1.5-fold molar excess) and intensities of assigned RRM resonances were measured with (I) and without (I_0) irradiation in aliphatic region.

(B) Ribbon (left) and surface (middle and right) representations of the RRM (PDB: 1LCW; green), showing binding sites for Kapβ2 (magenta, residues with I/I_0 <0.4 in cross saturation experiment) and RNA (yellow).

(C) Same as (A), but shown here are I/I_0 of assigned ZnF domain non-proline resonances in FUS(164-500) in the cross saturation transfer experiment.

(D) Selected resonances of RRM (green) and ZnF (orange) domains from ^{1}H/^{15}N TROSY HSQC (left panels, cross saturation transfer) and ^{1}H/^{15}N HSQC (right panels, line broadening) NMR spectra of ^{15}N-FUS(164-500) showing change in intensity in cross saturation and line broadening experiments upon addition of 3-fold molar excess Kapβ2-M9M.

(E) Homology model of the FUS ZnF domain (orange; from ZnF in ZNF265, PDB: 2K1P). Ribbon (left) and surface (middle and right) representations showing binding sites for Kapβ2 (magenta, residues with I/I_0 <0.55 in cross saturation experiment) and RNA (yellow). Residues with unassigned/missing/proline resonances are in white.

Error bars in (A) and (C) represent errors propagated from the measurement of noise in the NMR spectra. See also Figure S4.

site, which would be occluded in the native FUS•Kapβ2 complex).

The ^{1}H/^{15}N HSQC spectrum of 17 μM ^{15}N-FUS(164-500) shows many strong resonances with ^{1}H chemical shifts between ~7.5 ppm and 8.5 ppm, mostly representing residues in unstructured regions of the protein, as well as numerous resonances outside of this window, which represent the folded RRM (residues 285–370) and Cys4-type ZnF (residues 421–455) domains

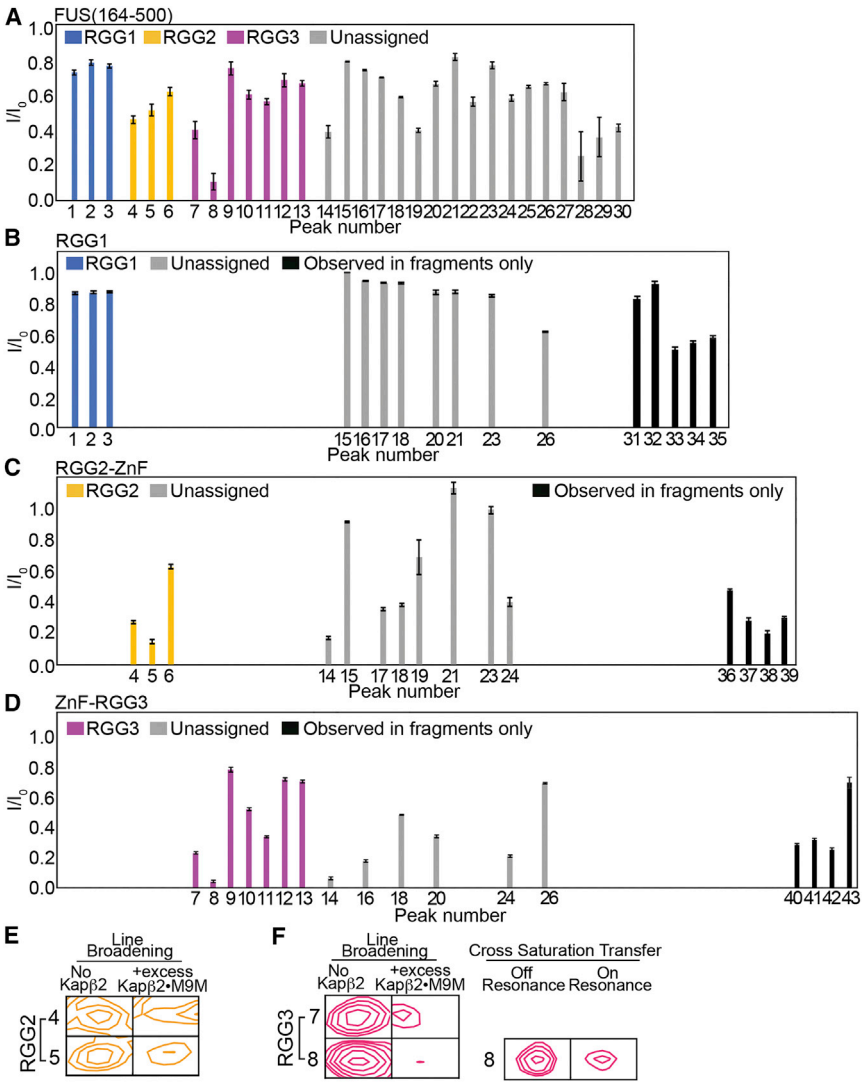

Figure 5. Kapβ2 Interacts with Disordered RGG Regions

(A–D) Attenuation of glycine resonances in $^{1}H/^{15}N$ HSQC NMR spectra of ^{15}N-FUS(164-500) (A), RGG1 (B), RGG2-ZnF (C), and ZnF-RGG3 (D) upon addition of 2-fold molar excess of Kapβ2•M9M.

(E and F) Selected glycine amide resonances of RGG2 (E) and RGG3 (F, left) in $^{1}H/^{15}N$ HSQC spectra ± 2-fold molar excess Kapβ2•M9M. (F) Right: selected glycine amide resonances of RGG3 in $^{1}H/^{15}N$ TROSY-based cross saturation transfer experiments in the presence of a 1.5-fold molar excess of Kapβ2•M9M with off- or on-resonance saturation. Cross saturation experiment was performed on $^{2}H/^{15}N$-FUS(164-500) complexed with unlabeled Kapβ2•M9M in 1:1.5 molar ratio. Error bars in (A–D) represent errors propagated from the measurement of noise in the NMR spectra.

See also Figure S5 and Tables S2 and S3.

(Figure S4B; Tables S2 and S3). Correspondence between the dispersed resonances and reported chemical shift assignments of the two domains (Iko et al., 2004; Liu et al., 2013) enabled us to assign most resonances from the RRM and ZnF to specific residues (Figures 4A, 4C, and S4B).

In cross saturation transfer experiments, minimal changes were observed in amide resonances of $^{15}N/^{2}H$-labeled FUS(164-500) alone (not shown). In the presence of 1.5-fold excess Kapβ2•M9M, a subset of amide resonances in the RRM domain showed particularly large decreases in intensity (>60%; Figures 4A and 4D). These resonances mapped to a contiguous patch on one face of the FUS RRM domain (PDB: 2LCW) (Liu et al., 2013) defined by its two α helices (Figure 4B). Similarly, we observed greater decreases in intensity (>45%) of certain resonances in the ZnF domain (Figures 4C and 4D). These resonances mapped to one face of a homology model of the FUS ZnF (PDB: 2K1P) (Iko et al., 2004; Loughlin et al., 2009), defined by its C-terminal β strand (Figure 4E). Although the uncertainties in intensity ratio (saturated versus unsaturated) for any individual peak is relatively large due to the broad lines induced by Kapβ2, the convergence of the affected residues to contiguous patches affords confidence that they map contact sites on the RRM and ZnF domains.

As in our analysis of the LC region, we also examined line broadening of FUS resonances upon addition of 3-fold excess Kapβ2•M9M. As detailed in Figures S4C–S4G, similar, although more extensive, regions of the RRM and ZnF domains were also perturbed by Kapβ2 addition in these experiments. Thus, the cross saturation transfer and line broadening data indicate that in the absence of high-affinity Kapβ2-PY-NLS binding, the RRM and ZnF domains can make weak direct contacts to regions of the karyopherin outside of its PY-NLS binding site.

Analysis of the unfolded RGG regions of FUS(164-500) was complicated by the low sequence complexity of these elements, which produces severe overlap in $^{1}H/^{15}N$ correlation spectra. Of the 146 glycine residues in the three regions, only 30 distinct peaks could be observed in the glycine region of the spectra (105–111 ^{15}N ppm) (Figure 5A). The glycine resonances appear to be present but overlapped, rather than absent due to line broadening, based on spectra of fragments containing individual RGG elements (RGG1 alone, RGG2-ZnF, and ZnF-RGG3). That is, there are many instances of peaks with identical chemical shifts appearing in spectra of different fragments, and the fragment spectra are largely subsets of the FUS(164-500) spectrum (Figures 5A–5F and S5A–S5D). In cross saturation transfer experiments of $^{15}N/^{2}H$-FUS(164-500) plus excess Kapβ2•M9M, only one of the 30 distinct glycine peaks, peak 8, decreased (Figure 5F). This peak could be assigned to RGG3 based on comparison to spectra of the fragments (Figure S5D).

A

SAXS analysis of FUS and Kapβ2

Protein	MBP	MBP-FUS	Kapβ2	Kapβ2•FUS	Kapβ2•MBP-FUS
Molecular weight (kDa)	42.6	96.0	98.1	151.5	194.1
R_g^{SAXS} (Å)	25.8	48.7	37.3	45.3	58.1
$R_g^{Globular}$ (Å)	23.0	30.2	30.4	35.1	38.1
$R_g^{SAXS}/R_g^{Globular}$	1.12	1.61	1.23	1.29	1.52
D_{max} (Å)	84.6	205.0	122.4	156.3	199.6
D_{max}/R_g^{SAXS}	3.28	4.21	3.28	3.45	3.44

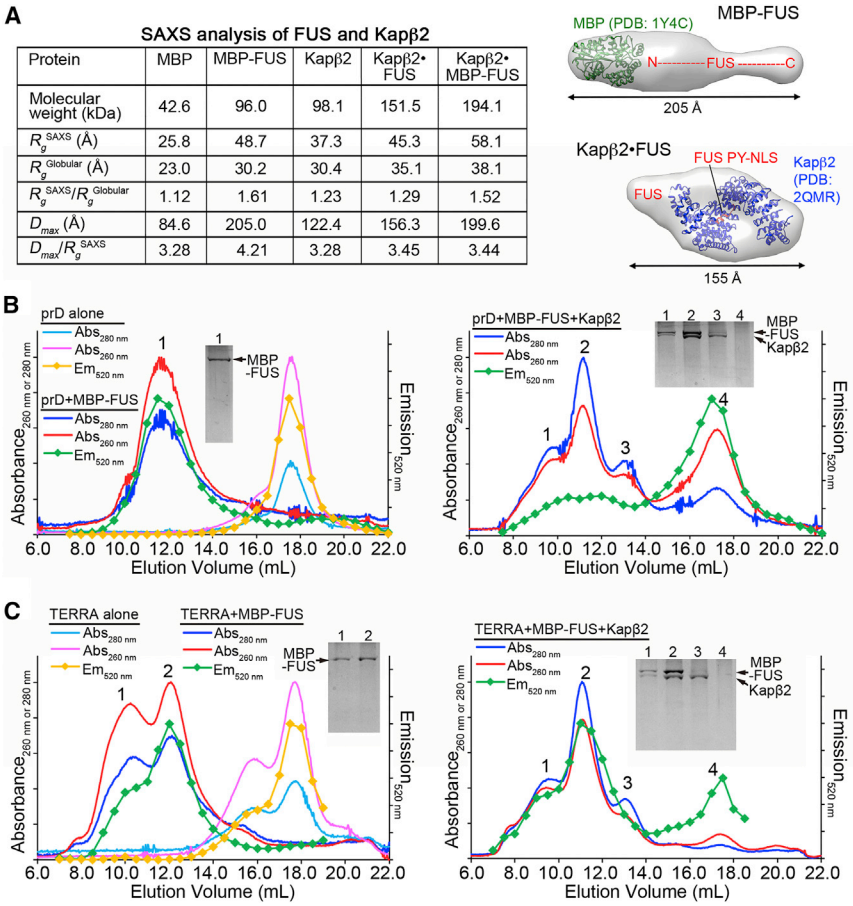

Figure 6. Implications of Kapβ2 Binding to Multiple Sites across FUS: SAXS Analysis and RNA-Binding

(A) SAXS profiles of MBP, MBP-FUS, Kapβ2, Kapβ2•FUS, and Kapβ2•MBP-FUS produced radius of gyration R_g^{SAXS}, maximum particle size D_{max}, and pair distribution function P(r). $R_g^{Globular}$ was estimated using the formula of $6.6*MW^{0.333}$ Å. Right: *ab initio* shapes of MBP-FUS and Kapβ2•FUS with the structures of MBP (PDB: 1Y4C), Kapβ2 (PDB: 2QMR), and the FUS PY-NLS (Figures S2F and S2G) coarsely fitted to the SAXS envelopes. See also Figure S6 and Table S4.

(B) Size exclusion chromatography (monitored by $Abs_{280\ nm}$, $Abs_{260\ nm}$ and fluorescence emission at 520 nm [$Em_{520\ nm}$]) of 1 μM prD RNA alone and 1 μM prD + 3 μM MBP-FUS (left), and of 1 μM prD + 3 μM MBP-FUS + 3.2 μM Kapβ2 (right).

(C) Size exclusion chromatography as in (B) of 2 μM TERRA RNA alone and 2 μM TERRA + 3 μM MBP-FUS (left), and 2 μM TERRA + 3 μM MBP-FUS + 3.2 μM Kapβ2 (right). 5′ of the RNAs were labeled with 6-FAM fluorophore and proteins were visualized by Coomassie blue-stained SDS/PAGE.

In line-broadening experiments, several glycine peaks in FUS(164-500) decreased in intensity upon addition of excess Kapβ2 (Figure 5A). Comparison to the RGG fragments allowed some of these to be assigned to RGG2 and others to RGG3 (Figures 5A, S5C, and S5D). In analogous experiments involving the RGG2-ZnF and ZnF-RGG3 fragments, these same peaks plus others broadened upon Kapβ2 addition (Figures 5C and 5D). In spectra of these fragments and of FUS(164-500), the chemical shifts of ZnF resonances are identical within experimental error to those of the isolated domain (Figure S5F), suggesting that there are no intramolecular contacts of the RGG regions with the ZnF domain (see Figure S5F legend for a more detailed discussion). Thus, the line broadening most likely represents direct Kapβ2 binding to RGG2 and RGG3. RGG1 may also make direct contacts, based on line broadening observed in spectra of isolated RGG1 plus Kapβ2•M9M (Figure 5B), although this is less certain because RGG1 resonances are severely overlapped in spectra of FUS(164-500). Consistent with binding of RGG regions, a number of unassigned resonances representing non-glycine residues in the unfolded region of the spectra of FUS(164-500) also broadened upon Kapβ2 addition (Figure S5G). We note that the most severely broadened glycine peak (#8) was the same as that affected in the cross saturation transfer experiment, showing consistency between the experiments (Figure 5F). Inefficient cross saturation transfer between Kapβ2 and the RGG2/3 regions probably results from a combination of low bound populations of individual Arg-$(Gly)_n$ or $(Gly)_n$ motifs and binding dynamics that are unfavorable to the experiment.

The combined NMR data show that Kapβ2 binds to the N-terminal LC region (Figure 3B) as well as large portions of the FUS C-terminal segment (Figures 4A–4E and 5A–5F), including the RGG2 and RGG3 regions, the RRM and ZnF domains.

Implications of Kapβ2 Binding across FUS: SAXS Analysis and RNA-Binding

Small angle X-ray scattering (SAXS) analysis shows substantial compaction of full-length FUS upon binding Kapβ2. Five SAXS profiles (MBP, MBP-FUS, Kapβ2, Kapβ2•FUS, and Kapβ2•MBP-FUS) were analyzed to calculate radius of gyration (R_g^{SAXS}), maximum particle size (D_{max}), and pair distribution function (P(r)) (Figure 6A) (Franke et al., 2017). According to the molecular weight estimation from SAXS analysis (Table S4), the polydispersity of MBP-FUS is highly concentration-dependent. Thus, the parameters in Figure 6A were calculated from the merged SAXS profiles, where polydispersity of MBP-FUS (and other samples tested) is negligible (Kikhney and Svergun, 2015). To assess compactness of the SAXS samples, $R_g^{Globular}$ was estimated using a formula of $6.6*MW^{0.333}$ Å (for MW in kDa) (Erickson, 2009). MBP-FUS presents the largest values of $R_g^{SAXS}/R_g^{Globular}$, D_{max}, and D_{max}/R_g^{SAXS}, suggesting that FUS is significantly expanded/extended in solution compared to globular proteins. In contrast, Kapβ2•FUS presents smaller values of $R_g^{SAXS}/R_g^{Globular}$, D_{max}, and D_{max}/R_g^{SAXS}, suggesting that FUS becomes more compact upon binding Kapβ2.

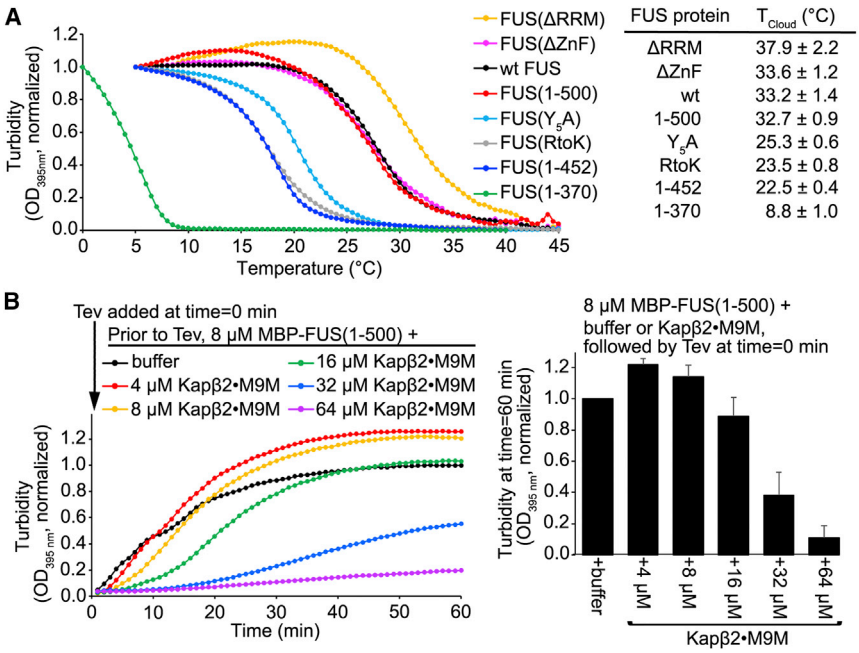

FUS protein	T_{Cloud} (°C)
ΔRRM	37.9 ± 2.2
ΔZnF	33.6 ± 1.2
wt	33.2 ± 1.4
1-500	32.7 ± 0.9
Y_5A	25.3 ± 0.6
RtoK	23.5 ± 0.8
1-452	22.5 ± 0.4
1-370	8.8 ± 1.0

Figure 7. Regions of FUS that Bind Kapβ2 Contribute to Phase Separation

(A) Temperature dependence of FUS phase separation. Turbidity (OD_{395nm}) of 8 μM MBP-FUS proteins (wild-type [WT] and FUS mutants) after 3 hr treatment with Tev protease was monitored as temperatures were decreased from 40°C or 45°C to 0°C or 5°C. Optical densities were normalized to values measured at 0°C or 5°C. T_{Cloud} is the x-intercept of tangent at inflection point of the curve (mean of 3 technical replicates, ± SD).

(B) Left: turbidity of 8 μM MBP-FUS(1-500), in the presence of buffer or 4–64 μM Kapβ2•M9M, measured for 60 min at room temperature after treatment with Tev protease. Right: turbidity at time = 60 min of experiments in the left panel, normalized to FUS turbidity in the presence of buffer (mean of 3 technical replicates, ± SD).

See also Figure S7.

Consistently, the *ab initio* shapes computed from the experimental SAXS profiles (Figures 6A and S6A–S6E), as well as the pair distribution functions (Figure S6F) further support the compactness of FUS upon binding Kapβ2 (similar in buffers with 5% or 20% glycerol; Figure S6G).

The RGG regions and ZnF and RRM domains were previously shown to bind RNA. The ZnF and RRM domains bind weakly to GGUG-containing RNA, with K_D values in the micromolar range (Iko et al., 2004; Ozdilek et al., 2017). In contrast, the RGG regions bind RNA with K_D values in the nanomolar range. We examined the effects of Kapβ2 on FUS binding to two RNAs, the 48-nt prD (DNMT) RNA (K_D ~0.7 μM; binds RGG1 and RGG3) and the 24-nt telomeric repeat TERRA RNA (K_D ~12 nM; binds RGG3) (Ozdilek et al., 2017; Takahama and Oyoshi, 2013). Figures 6B and 6C show MBP-FUS binding to fluorophore-labeled prD and TERRA, respectively. Addition of Kapβ2 to the MBP-FUS•RNA complexes caused efficient release of prD, but only partial release of the higher affinity TERRA, consistent with overlapping binding sites in the FUS RGG regions. Because RNA promotes aggregation and LLPS of FUS (Burke et al., 2015; Schwartz et al., 2013), our data also suggest that Kapβ2 may inhibit biological phase separation of FUS through blocking interactions with RNA.

Regions of FUS that Bind Kapβ2 Contribute to LLPS

We examined the temperature dependence of LLPS of full-length FUS and a series of deletion mutants to identify functionally important regions. At 8 μM, FUS phase separates at temperatures below 33°C (cloud point temperature, T_{cloud}), as assessed by a sharp increase in turbidity when temperature is decreased slowly from 45°C (Figure 7A). Removal of the PY-NLS did not affect LLPS (FUS(1-500) T_{cloud} 33°C; Figure 7A), consistent with observations that the PY-NLS does not affect FUS aggregation (Ju et al., 2011; Sun et al., 2011).

Our NMR data suggest that Kapβ2 contacts three segments of the FUS LC (Figures 3B and S3B). Alanine mutation of the five tyrosines in these segments (Tyr38, Tyr 41, Tyr97, Tyr100, and Tyr149) in full-length FUS (FUS(Y_5A)) substantially decreased T_{cloud} to 25°C (Figure 7A), consistent with the importance of tyrosine side chains in self-assembly of the FUS LC region (Kato et al., 2012; Lin et al., 2017), and in LLPS of disordered proteins in general (Banani et al., 2017; Brangwynne et al., 2015).

Deletion of the RRM or ZnF domain (FUS(ΔRRM) or FUS(ΔZnF)) does not decrease the ability of FUS to phase-separate. The T_{cloud} of 33.6°C for FUS(ΔZnF) is similar to that of wild-type FUS, while the T_{cloud} of 38°C for FUS(ΔRRM) suggests an enhancement in phase separation (Figure 7A). As described in Figures 5A, S5A, S5B, S5E, S7A, and S7B, enhancement of LLPS by RRM deletion appears to derive from loss of inhibitory intramolecular interactions between the domain and RGG regions (see below).

We made several mutants to perturb the FUS RGG regions. Mutating all arginine residues in RGG2 and RGG3 of full-length FUS to lysines (FUS(RtoK)) decreased T_{cloud} to 23.5°C (Figure 7A) suggesting stereospecific roles of arginine side chains in promoting LLPS. The FUS(1-452) truncation mutant has a similarly low T_{cloud} of 22.5°C indicating the importance of RGG3 in LLPS (Figure 7A). The last mutant, FUS(1-370), lacks both RGG2 and RGG3 and shows a drastic decrease in its ability to phase separate (T_{cloud} of 8°C).

At 2 μM, wild-type FUS and the mutants showed the same trends in LLPS as at 8 μM, but T_{cloud} was uniformly decreased as expected from theory (Figure S7C). We also observed the same patterns in temperature-dependent analyses of LLPS by fluorescence microscopy, with FUS(ΔRRM) > FUS wild-type > FUS(1-452) in their propensity to phase separate (Figure S7D). Together, these studies show that the LC and RGGs regions are the main determinants of FUS LLPS.

As detailed below, our combined data lead to a model in which FUS is anchored to Kapβ2 through high-affinity interactions of the PY-NLS. This enables distributed weak interactions to disrupt FUS self-association and phase separation. A prediction of this model is that even in the absence of the Kapβ2-PY-NLS interactions, high concentrations of the karyopherin should disrupt FUS phase separation. Consistent with this prediction, we found that very high concentrations (64 μM) of Kapβ2•M9M are able to inhibit phase separation of FUS(1-500), which lacks the PY-NLS (Figure 7B).

DISCUSSION

Kapβ2 is the dominant nuclear transport factor that traffics FUS into the nucleus (Dormann and Haass, 2011). This activity is based on high-affinity, RanGTP-sensitive binding of Kapβ2 to the PY-NLS of FUS (Lee et al., 2006; Zhang and Chook, 2012). Here, we describe an additional biochemical consequence of this interaction—disruption of LLPS of FUS. Mechanistic studies show that in addition to the established high-affinity binding of Kapβ2 to the FUS PY-NLS, regions outside of the PY-NLS binding pocket of the karyopherin make weak, distributed interactions with multiple regions of FUS. These regions include tyrosine-repeats in the LC region, the RGG elements, and the folded RRM and zinc finger domains. Of these FUS elements, the LC and RGG regions contribute to LLPS. Thus, heterotypic Kapβ2-FUS interactions should compete with homotypic FUS-FUS interactions. Because the drive for phase-separation is distributed across the FUS sequence, it seems logical that Kapβ2 binds in distributed fashion to block phase separation. Our data suggest a model where high-affinity and stable tethering of Kapβ2 to the FUS PY-NLS enables weak and dynamic interactions involving other regions of the two proteins, which block formation of higher-order FUS assemblies and phase separation.

Within the complex, it is possible that Kapβ2 engages all sites on FUS simultaneously. Alternatively the complex may be dynamic in nature, sampling different collection of contacts that rapidly interconvert, as observed in other IDP interactions, for example the binding of disordered cyclin-dependent kinase (CDK) inhibitor Sic1 to its receptor Cdc4 (Mittag et al., 2008). Based on structural and energetic considerations, we favor the latter model of a dynamic complex. The regions of Kapβ2 that bind the different FUS elements remain unknown. However, features of the karyopherin that are conserved among other β-importin proteins suggest potential modes of interaction. First, Kapβ2 possesses a series of hydrophobic patches on the convex spine of its superhelical structure (Chook and Suel, 2011; Conti and Izaurralde, 2001) (Figure S7E). During nuclear import, these patches bind in dynamic fashion to the large arrays of FG repeats in the nuclear pore complex. These same regions could be repurposed to make analogous interactions with tyrosine repeats in the FUS LC region. In addition, Kapβ2 possess highly acidic surfaces and adjacent long acidic loops on the concave side of its superhelix. Portions of these acidic elements bind to the FUS PY-NLS, but parts remain solvent-exposed in the complex (Figure S7E) and could interact with the basic RGG regions of FUS. Interactions with these spatially distributed surfaces on Kapβ2 significantly constrain the FUS chain, as evidenced by our SAXS data showing compaction of the extended FUS upon binding the karyopherin.

In addition to FUS, Kapβ2 binds and imports many PY-NLS containing, RNA-binding proteins including EWS, TAF15, hnRNP A1, and hnRNP A2. Like FUS, these proteins contain folded RNA binding domains, as well as LC and RGG regions, and are found in RNA granules (King et al., 2012). As shown in the companion paper by Guo et al. (this issue of Cell), high-affinity binding of Kapβ2 to the PY-NLSs of these proteins prevents their self-association and likely phase separation. Although the Kapβ2 cargos have different domain arrangements, in all cases individual elements are either disordered or connected by flexible linkers. Thus, Kapβ2 can probably contact the RGG and LC regions of the cargos when anchored to their PY-NLSs, disrupting self-association through a mechanism analogous to that of FUS.

In addition to Kapβ2, other β-importin family members may also act to modulate phase separation of LC-containing RNA-binding proteins. We have shown here that two other importins can inhibit LLPS by FUS when the protein is equipped with high-affinity recognition peptides. β-importin family members share both the hydrophobic patches on the convex spine and the acid surfaces and loops on their concave side, which are likely important in disruption of LLPS by FUS (Chook and Suel, 2011; Conti and Izaurralde, 2001) (Figure S7E). These same elements could be used to disrupt LLPS by other RNA-binding proteins. While conceptually similar, this molecular mechanism is distinct from that proposed previously to account for the chaperone activity of importins toward positively charged cargo proteins (Jakel et al., 2002). In contrast to importins, exportins such as CRM1 have very different charge distributions and spatial relationships between NES- and FG-binding sites (Dong et al., 2009; Fung and Chook, 2014; Port et al., 2015). Unlike the large contiguous negatively charged surfaces on the concave side of importins, analogous surfaces of exportins are basic (Figures S7E and S7F). Further, in contrast to NLSs, which bind the concave acidic surfaces of importins, the NES binds in a hydrophobic groove that is located on the FG-repeats-binding convex surface of CRM1 (Figures S7E and S7F). Thus, conserved features enable importins to disrupt LLPS of RNA binding proteins that possess appropriate NLSs, an activity that is likely not shared by exportins resembling CRM1.

We can envision several potential mechanisms by which the ability of Kapβ2 to control FUS LLPS could be important in cell physiology. First, Kapβ2 may bind newly translated FUS and prevent it from phase separating in the cytoplasm while escorting it into the nucleus. Kapβ2-FUS interactions may also modulate cytoplasmic RNA granules, where FUS is localized upon heat shock or other cellular stresses (Dormann et al., 2010; Li et al., 2013; Patel et al., 2015). In this role, Kapβ2 may facilitate dissociation of FUS from RNA, controlling dynamics of the protein and/or its stoichiometry in the condensates. If FUS is important to granule stability, Kapβ2 could control granule formation and/or disassembly, as we observed here. Finally, by weakening intermolecular contacts, substoichiometric amounts of Kapβ2 could modulate the material properties of granules, likely affecting the chemistry that occurs within them (Banani et al., 2017; Guo et al., 2018; Hofweber et al., 2018). In conclusion,

our data suggest an expanded role for β-importins. Not only do they traffic proteins into the nucleus, they also may control the formation, composition, and dynamics of biomolecular condensates.

STAR★METHODS

Detailed methods are provided in the online version of this paper and include the following:

- KEY RESOURCES TABLE
- CONTACT FOR REAGENT AND RESOURCE SHARING
- EXPERIMENTAL MODEL AND SUBJECT DETAILS
- METHOD DETAILS
  - Constructs, protein expression and purification
  - Turbidity Assays
  - Monitoring interactions between Importins and FUS
  - Monitoring the effects of Kapβ2 on FUS-RNA interactions
  - Imaging of turbid FUS solution
  - Dynamic light scattering analysis
  - NMR analysis of FUS LC with Kapβ2
  - NMR analysis of FUS(164-526), FUS(164-500) and smaller FUS fragments with Kapβ2
  - Small-angle X-ray scattering (SAXS)
  - X-ray crystallography of Kapβ2•FUS complexes
- QUANTIFICATION AND STATISTICAL ANALYSIS
- DATA AND SOFTWARE AVAILABILITY

SUPPLEMENTAL INFORMATION

Supplemental Information includes seven figures, four tables, and three videos and can be found with this article online at https://doi.org/10.1016/j.cell.2018.03.003.

ACKNOWLEDGMENTS

We thank D. Dormann and J. Shorter for critical reading of the manuscript. We thank A. Patel and A. A. Hyman for their gift of FUS-GFP, T. Cagatay and A. Gonzalez for help subcloning, J. Hu and D. Corey for their help with temperature-dependent turbidity analysis, N. Conrad and K. Lynch for advice on FUS-RNA analysis, T. Matsui and T.M. Weiss at SSRL, SLAC National Accelerator Laboratory, for assistance with collecting SAXS data, and B. Raveh for discussions on SAXS analysis. We thank D. Tomchick for advice on X-ray structure determination, and the Structural Biology Laboratory and Macromolecular Biophysics Resource at UTSW for their assistance with crystallographic and biophysical data collection. Crystallographic results are derived from work performed at Argonne National Laboratory, Structural Biology Center at the Advanced Photon Source. Argonne is operated by UChicago Argonne, LLC, for the U.S. Department of Energy (DOE), Office of Biological and Environmental Research (BER) under contract DE-AC02-06CH11357. NMR data were obtained in part at the Brown University Structural Biology Core Facility supported by the Division of Biology and Medicine, Brown University. NMR spectroscopy at UTSW is supported by NIH instrumentation grants 1S10RR26461-1 and 1S10OD018027-01. SAXS experiments were performed at the SSRL, SLAC National Accelerator Laboratory operated for DOE by Stanford University. The SSRL SMBP is supported by the DOE BER, by the NIH, NCRR, Biomedical Technology Program (P41RR001209), and by NIGMS, NIH (P41GM103393). This work was funded by NIGMS of NIH under R01GM069909 (Y.M.C.), U01GM98256-01 (Y.M.C. and A.S.), R01GM56322 (M.K.R.), R01GM118530 (N.L.F.), R01GM083960, P41GM109824, and R01GM112108 (A.S), R01GM114274 (R.O.), T32GM008203 (J.J.), T32GM008297 (J.M.B.), the Howard Hughes Medical Institute HCIA grant (M.K.R.), the Welch Foundation grants I-1532 (Y.M.C.) and I-1544 (M.K.R.), Leukemia and Lymphoma Society Scholar Award (Y.M.C.), and the University of Texas Southwestern Endowed Scholars Program (Y.M.C.). Work in M.K.R.'s lab was supported by the Howard Hughes Medical Institute. R.A. was an American Heart Association Postdoctoral Fellow and H.Y.J.F was a Howard Hughes Medical Institute International Student Research fellow.

AUTHOR CONTRIBUTIONS

Conceptualization, Y.M.C. and M.K.R.; Methodology, Y.M.C., M.K.R., N.L.F., A.S., R.O., T.Y., and R.A.; Investigation, T.Y., R.A., J.J., H.Y.J.F., Y.M.C., M.K.R., K.A.B., Y.L., W.B.P., S.J.K., D.S., M.S., J.M.B., R.O., and N.L.F.; Writing—Original Draft, Y.M.C., M.K.R., Y.L., S.J.K., and N.L.F.; Writing—Review & Editing, Y.M.C., M.K.R., T.Y., and R.A.; Funding Acquisition, Y.M.C., M.K.R., R.O., A.S., and N.L.F.

DECLARATION OF INTERESTS

The authors declare no competing interests.

Received: April 13, 2017
Revised: November 29, 2017
Accepted: February 28, 2018
Published: April 19, 2018

REFERENCES

Adams, P.D., Afonine, P.V., Bunkoczi, G., Chen, V.B., Davis, I.W., Echols, N., Headd, J.J., Hung, L.W., Kapral, G.J., Grosse-Kunstleve, R.W., et al. (2010). PHENIX: a comprehensive Python-based system for macromolecular structure solution. Acta Crystallogr. D Biol. Crystallogr. *66*, 213–221.

Afonine, P.V., Grosse-Kunstleve, R.W., Echols, N., Headd, J.J., Moriarty, N.W., Mustyakimov, M., Terwilliger, T.C., Urzhumtsev, A., Zwart, P.H., and Adams, P.D. (2012). Towards automated crystallographic structure refinement with phenix.refine. Acta Crystallogr. D Biol. Crystallogr. *68*, 352–367.

Banani, S.F., Lee, H.O., Hyman, A.A., and Rosen, M.K. (2017). Biomolecular condensates: organizers of cellular biochemistry. Nat. Rev. Mol. Cell Biol. *18* (5), 285–298.

Brangwynne, C.P., Tompa, P., and Pappu, R.V. (2015). Polymer physics of intracellular phase transitions. Nat. Phys. *11*, 899–904.

Brautigam, C.A. (2015). Calculations and publication-quality illustrations for analytical ultracentrifugation data. Methods Enzymol. *562*, 109–133.

Brautigam, C.A., Zhao, H., Vargas, C., Keller, S., and Schuck, P. (2016). Integration and global analysis of isothermal titration calorimetry data for studying macromolecular interactions. Nat. Protoc. *11*, 882–894.

Burke, K.A., Janke, A.M., Rhine, C.L., and Fawzi, N.L. (2015). Residue-by-residue view of in vitro FUS granules that bind the C-terminal domain of RNA polymerase II. Mol. Cell *60*, 231–241.

Cansizoglu, A.E., and Chook, Y.M. (2007). Conformational heterogeneity of karyopherin beta2 is segmental. Structure *15*, 1431–1441.

Cansizoglu, A.E., Lee, B.J., Zhang, Z.C., Fontoura, B.M., and Chook, Y.M. (2007). Structure-based design of a pathway-specific nuclear import inhibitor. Nat. Struct. Mol. Biol. *14*, 452–454.

Chen, V.B., Arendall, W.B., 3rd, Headd, J.J., Keedy, D.A., Immormino, R.M., Kapral, G.J., Murray, L.W., Richardson, J.S., and Richardson, D.C. (2010). MolProbity: all-atom structure validation for macromolecular crystallography. Acta Crystallogr. D Biol. Crystallogr. *66*, 12–21.

Chook, Y.M., and Blobel, G. (1999). Structure of the nuclear transport complex karyopherin-beta2-Ran x GppNHp. Nature *399*, 230–237.

Chook, Y.M., and Suel, K.E. (2011). Nuclear import by karyopherin-betas: recognition and inhibition. Biochim. Biophys. Acta *1813*, 1593–1606.

Chook, Y.M., Jung, A., Rosen, M.K., and Blobel, G. (2002). Uncoupling Kapbeta2 substrate dissociation and ran binding. Biochemistry *41*, 6955–6966.

Connolly, B.D., Petry, C., Yadav, S., Demeule, B., Ciaccio, N., Moore, J.M., Shire, S.J., and Gokarn, Y.R. (2012). Weak interactions govern the viscosity of concentrated antibody solutions: high-throughput analysis using the diffusion interaction parameter. Biophys. J. *103*, 69–78.

Conti, E., and Izaurralde, E. (2001). Nucleocytoplasmic transport enters the atomic age. Curr. Opin. Cell Biol. *13*, 310–319.

Crozat, A., Aman, P., Mandahl, N., and Ron, D. (1993). Fusion of CHOP to a novel RNA-binding protein in human myxoid liposarcoma. Nature *363*, 640–644.

Delaglio, F., Grzesiek, S., Vuister, G.W., Zhu, G., Pfeifer, J., and Bax, A. (1995). NMRPipe: a multidimensional spectral processing system based on UNIX pipes. J. Biomol. NMR *6*, 277–293.

Dong, X., Biswas, A., Suel, K.E., Jackson, L.K., Martinez, R., Gu, H., and Chook, Y.M. (2009). Structural basis for leucine-rich nuclear export signal recognition by CRM1. Nature *458*, 1136–1141.

Dormann, D., and Haass, C. (2011). TDP-43 and FUS: a nuclear affair. Trends Neurosci. *34*, 339–348.

Dormann, D., Rodde, R., Edbauer, D., Bentmann, E., Fischer, I., Hruscha, A., Than, M.E., Mackenzie, I.R., Capell, A., Schmid, B., et al. (2010). ALS-associated fused in sarcoma (FUS) mutations disrupt Transportin-mediated nuclear import. EMBO J. *29*, 2841–2857.

Ederle, H., and Dormann, D. (2017). TDP-43 and FUS en route from the nucleus to the cytoplasm. FEBS Lett. *591*, 1489–1507.

Emsley, P., Lohkamp, B., Scott, W.G., and Cowtan, K. (2010). Features and development of Coot. Acta Crystallogr. D Biol. Crystallogr. *66*, 486–501.

Erickson, H.P. (2009). Size and shape of protein molecules at the nanometer level determined by sedimentation, gel filtration, and electron microscopy. Biol. Proced. Online *11*, 32–51.

Fischer, H., Neto, M.D., Napolitano, H.B., Polikarpov, I., and Craievich, A.F. (2010). Determination of the molecular weight of proteins in solution from a single small-angle X-ray scattering measurement on a relative scale. J. Appl. Cryst. *43*, 101–109.

Franke, D., Petoukhov, M.V., Konarev, P.V., Panjkovich, A., Tuukkanen, A., Mertens, H.D.T., Kikhney, A.G., Hajizadeh, N.R., Franklin, J.M., Jeffries, C.M., et al. (2017). ATSAS 2.8: a comprehensive data analysis suite for small-angle scattering from macromolecular solutions. J. Appl. Cryst. *50*, 1212–1225.

Fung, H.Y., and Chook, Y.M. (2014). Atomic basis of CRM1-cargo recognition, release and inhibition. Semin. Cancer Biol. *27*, 52–61.

Fung, H.Y., Fu, S.C., Brautigam, C.A., and Chook, Y.M. (2015). Structural determinants of nuclear export signal orientation in binding to exportin CRM1. eLife. https://doi.org/10.7554/eLife.10034.

Guex, N., Peitsch, M.C., and Schwede, T. (2009). Automated comparative protein structure modeling with SWISS-MODEL and Swiss-PdbViewer: A historical perspective. Electrophoresis *30*, S162–S173.

Guo, L., Kim, H.J., Wang, H., Monaghan, J., Freyermuth, F., Sung, J., O'Donovan, K., Fare, C., Diaz, Z., Singh, N., et al. (2018). Nuclear-Import Receptors Reverse Aberrant Phase Transitions of RNA-Binding Proteins with Prion-like Domains. Cell *173*. Published online April 19, 2018. https://doi.org/10.1016/j.cell.2018.03.002.

Harrison, A.F., and Shorter, J. (2017). RNA-binding proteins with prion-like domains in health and disease. Biochem. J. *474*, 1417–1438.

Hofweber, M., Hutten, S., Bourgeois, B., Spreitzer, E., Niedner-Boblenz, A., Schifferer, M., Ruepp, M.-D., Simons, M., Niessing, D., Madl, T., et al. (2018). Phase Separation of FUS Is Suppressed by Its Nuclear Import Receptor and Arginine Methylation. Cell *173*. Published online April 19, 2018. https://doi.org/10.1016/j.cell.2018.03.004.

Hough, L.E., Dutta, K., Sparks, S., Temel, D.B., Kamal, A., Tetenbaum-Novatt, J., Rout, M.P., and Cowburn, D. (2015). The molecular mechanism of nuclear transport revealed by atomic-scale measurements. eLife *4*, e10027.

Iko, Y., Kodama, T.S., Kasai, N., Oyama, T., Morita, E.H., Muto, T., Okumura, M., Fujii, R., Takumi, T., Tate, S., et al. (2004). Domain architectures and characterization of an RNA-binding protein, TLS. J. Biol. Chem. *279*, 44834–44840.

Jakel, S., Mingot, J.M., Schwarzmaier, P., Hartmann, E., and Gorlich, D. (2002). Importins fulfil a dual function as nuclear import receptors and cytoplasmic chaperones for exposed basic domains. EMBO J. *21*, 377–386.

Jayalakshmi, V., and Krishna, N.R. (2002). Complete relaxation and conformational exchange matrix (CORCEMA) analysis of intermolecular saturation transfer effects in reversibly forming ligand-receptor complexes. J. Magn. Reson. *155*, 106–118.

Ju, S., Tardiff, D.F., Han, H., Divya, K., Zhong, Q., Maquat, L.E., Bosco, D.A., Hayward, L.J., Brown, R.H., Jr., Lindquist, S., et al. (2011). A yeast model of FUS/TLS-dependent cytotoxicity. PLoS Biol. *9*, e1001052.

Kato, M., Han, T.W., Xie, S., Shi, K., Du, X., Wu, L.C., Mirzaei, H., Goldsmith, E.J., Longgood, J., Pei, J., et al. (2012). Cell-free formation of RNA granules: low complexity sequence domains form dynamic fibers within hydrogels. Cell *149*, 753–767.

Kikhney, A.G., and Svergun, D.I. (2015). A practical guide to small angle X-ray scattering (SAXS) of flexible and intrinsically disordered proteins. FEBS Lett. *589*, 2570–2577.

Kim, S.J., Fernandez-Martinez, J., Sampathkumar, P., Martel, A., Matsui, T., Tsuruta, H., Weiss, T.M., Shi, Y., Markina-Inarrairaegui, A., Bonanno, J.B., et al. (2014). Integrative structure-function mapping of the nucleoporin Nup133 suggests a conserved mechanism for membrane anchoring of the nuclear pore complex. Mol. Cell. Proteomics *13*, 2911–2926.

King, O.D., Gitler, A.D., and Shorter, J. (2012). The tip of the iceberg: RNA-binding proteins with prion-like domains in neurodegenerative disease. Brain Res. *1462*, 61–80.

Kobayashi, J., and Matsuura, Y. (2013). Structural basis for cell-cycle-dependent nuclear import mediated by the karyopherin Kap121p. J. Mol. Biol. *425*, 1852–1868.

Lee, B.J., Cansizoglu, A.E., Suel, K.E., Louis, T.H., Zhang, Z., and Chook, Y.M. (2006). Rules for nuclear localization sequence recognition by karyopherin beta 2. Cell *126*, 543–558.

Li, Y.R., King, O.D., Shorter, J., and Gitler, A.D. (2013). Stress granules as crucibles of ALS pathogenesis. J. Cell Biol. *201*, 361–372.

Lin, Y., Protter, D.S., Rosen, M.K., and Parker, R. (2015). Formation and maturation of phase-separated liquid droplets by RNA-binding proteins. Mol. Cell *60*, 208–219.

Lin, Y., Currie, S.L., and Rosen, M.K. (2017). Intrinsically disordered sequences enable modulation of protein phase separation through distributed tyrosine motifs. J. Biol. Chem. *292*, 19110–19120.

Liu, X.H., Niu, C.Y., Ren, J.T., Zhang, J.Y., Xie, X.D., Zhu, H.N., Feng, W., and Gong, W.M. (2013). The RRM domain of human fused in sarcoma protein reveals a non-canonical nucleic acid binding site. Biochem. Biophys, Acta *1832*, 375–385.

Loughlin, F.E., Mansfield, R.E., Vaz, P.M., McGrath, A.P., Setiyaputra, S., Gamsjaeger, R., Chen, E.S., Morris, B.J., Guss, J.M., and Mackay, J.P. (2009). The zinc fingers of the SR-like protein ZRANB2 are single-stranded RNA-binding domains that recognize 5′ splice site-like sequences. Proc. Natl. Acad. Sci. USA *106*, 5581–5586.

Milles, S., Mercadante, D., Aramburu, I.V., Jensen, M.R., Banterle, N., Koehler, C., Tyagi, S., Clarke, J., Shammas, S.L., Blackledge, M., et al. (2015). Plasticity of an ultrafast interaction between nucleoporins and nuclear transport receptors. Cell *163*, 734–745.

Minor, W., Cymborowski, M., Otwinowski, Z., and Chruszcz, M. (2006). HKL-3000: the integration of data reduction and structure solution–from diffraction images to an initial model in minutes. Acta Crystallogr. D Biol. Crystallogr. *62*, 859–866.

Mittag, T., Orlicky, S., Choy, W.Y., Tang, X., Lin, H., Sicheri, F., Kay, L.E., Tyers, M., and Forman-Kay, J.D. (2008). Dynamic equilibrium engagement of a polyvalent ligand with a single-site receptor. Proc. Natl. Acad. Sci. USA *105*, 17772–17777.

Molliex, A., Temirov, J., Lee, J., Coughlin, M., Kanagaraj, A.P., Kim, H.J., Mittag, T., and Taylor, J.P. (2015). Phase separation by low complexity domains

promotes stress granule assembly and drives pathological fibrillization. Cell *163*, 123–133.

Monahan, Z., Ryan, V.H., Janke, A.M., Burke, K.A., Rhoads, S.N., Zerze, G.H., O'Meally, R., Dignon, G.L., Conicella, A.E., Zheng, W., et al. (2017). Phosphorylation of the FUS low-complexity domain disrupts phase separation, aggregation, and toxicity. EMBO J. *36*, 2951–2967.

Murakami, T., Qamar, S., Lin, J.Q., Schierle, G.S., Rees, E., Miyashita, A., Costa, A.R., Dodd, R.B., Chan, F.T., Michel, C.H., et al. (2015). ALS/FTD mutation-induced phase transition of FUS liquid droplets and reversible hydrogels into irreversible hydrogels impairs RNP granule function. Neuron *88*, 678–690.

Murray, D.T., Kato, M., Lin, Y., Thurber, K.R., Hung, I., McKnight, S.L., and Tycko, R. (2017). Structure of FUS protein fibrils and its relevance to self-assembly and phase separation of low-complexity domains. Cell *171*, 615–627.

Ohshima, T., Nakajima, T., Oishi, T., Imamoto, N., Yoneda, Y., Fukamizu, A., and Yagami, K. (1999). CRM1 mediates nuclear export of nonstructural protein 2 from parvovirus minute virus of mice. Biochem. Biophys. Res. Commun. *264*, 144–150.

Oldenbourg, R. (1991). Analysis of edge birefringence. Biophys. J. *60*, 629–641.

Oldenbourg, R., and Mei, G. (1995). New polarized light microscope with precision universal compensator. J. Microsc. *180*, 140–147.

Ozdilek, B.A., Thompson, V.F., Ahmed, N.S., White, C.I., Batey, R.T., and Schwartz, J.C. (2017). Intrinsically disordered RGG/RG domains mediate degenerate specificity in RNA binding. Nucleic Acids Res. *45*, 7984–7996.

Patel, A., Lee, H.O., Jawerth, L., Maharana, S., Jahnel, M., Hein, M.Y., Stoynov, S., Mahamid, J., Saha, S., Franzmann, T.M., et al. (2015). A liquid-to-solid phase transition of the ALS protein FUS accelerated by disease mutation. Cell *162*, 1066–1077.

Pervushin, K., Riek, R., Wider, G., and Wüthrich, K. (1997). Attenuated T2 relaxation by mutual cancellation of dipole–dipole coupling and chemical shift anisotropy indicates an avenue to NMR structures of very large biological macromolecules in solution. Proceedings of the National Academy of Sciences *94*, 12366–12371.

Petoukhov, M.V., Franke, D., Shkumatov, A.V., Tria, G., Kikhney, A.G., Gajda, M., Gorba, C., Mertens, H.D., Konarev, P.V., and Svergun, D.I. (2012). New developments in the ATSAS program package for small-angle scattering data analysis. J. Appl. Crystallogr *45*, 342–350.

Port, S.A., Monecke, T., Dickmanns, A., Spillner, C., Hofele, R., Urlaub, H., Ficner, R., and Kehlenbach, R.H. (2015). Structural and functional characterization of CRM1-Nup214 interactions reveals multiple FG-binding sites involved in nuclear export. Cell Rep. *13*, 690–702.

Ryu, H.H., Jun, M.H., Min, K.J., Jang, D.J., Lee, Y.S., Kim, H.K., and Lee, J.A. (2014). Autophagy regulates amyotrophic lateral sclerosis-linked fused in sarcoma-positive stress granules in neurons. Neurobiol. Aging *35*, 2822–2831.

Scheuermann, T.H., and Brautigam, C.A. (2015). High-precision, automated integration of multiple isothermal titration calorimetric thermograms: new features of NITPIC. Methods *76*, 87–98.

Schrodinger, LLC (2015). The PyMOL Molecular Graphics System, Version 1.8. (Schrodinger, LLC).

Schwartz, J.C., Wang, X., Podell, E.R., and Cech, T.R. (2013). RNA seeds higher-order assembly of FUS protein. Cell Rep. *5*, 918–925.

Schwartz, J.C., Cech, T.R., and Parker, R.R. (2015). Biochemical properties and biological functions of FET proteins. Annu. Rev. Biochem. *84*, 355–379.

Soniat, M., and Chook, Y.M. (2016). Karyopherin-beta2 recognition of a PY-NLS variant that lacks the proline-tyrosine motif. Structure *24*, 1802–1809.

Sun, Z., Diaz, Z., Fang, X., Hart, M.P., Chesi, A., Shorter, J., and Gitler, A.D. (2011). Molecular determinants and genetic modifiers of aggregation and toxicity for the ALS disease protein FUS/TLS. PLoS Biol. *9*, e1000614.

Takahama, K., and Oyoshi, T. (2013). Specific binding of modified RGG domain in TLS/FUS to G-quadruplex RNA: tyrosines in RGG domain recognize 2′-OH of the riboses of loops in G-quadruplex. J. Am. Chem. Soc. *135*, 18016–18019.

Ueda, T., Takeuchi, K., Nishida, N., Stampoulis, P., Kofuku, Y., Osawa, M., and Shimada, I. (2014). Cross-saturation and transferred cross-saturation experiments. Q. Rev. Biophys. *47*, 143–187.

Vranken, W.F., Boucher, W., Stevens, T.J., Fogh, R.H., Pajon, A., Llinas, M., Ulrich, E.L., Markley, J.L., Ionides, J., and Laue, E.D. (2005). The CCPN data model for NMR spectroscopy: development of a software pipeline. Proteins *59*, 687–696.

Xiang, S.H., Kato, M., Wu, L.C., Lin, Y., Ding, M., Zhang, Y.J., Yu, Y.H., and McKnight, S.L. (2015). The LC domain of hnRNPA2 adopts similar conformations in hydrogel polymers, liquid-like droplets, and nuclei. Cell *163*, 829–839.

Zhang, Z.C., and Chook, Y.M. (2012). Structural and energetic basis of ALS-causing mutations in the atypical proline-tyrosine nuclear localization signal of the Fused in Sarcoma protein (FUS). Proc. Natl. Acad. Sci. USA *109*, 12017–12021.

Zhao, H., Piszczek, G., and Schuck, P. (2015). SEDPHAT–a platform for global ITC analysis and global multi-method analysis of molecular interactions. Methods *76*, 137–148.

STAR★METHODS

KEY RESOURCES TABLE

REAGENT or RESOURCE	SOURCE	IDENTIFIER
Chemicals, Peptides, and Recombinant Proteins		
HEPES	RPI	Cat#H75030-500.0
Sodium chloride	RPI	Cat#S23020-5000.0
Potassium chloride	Sigma	Cat#P9541-1158
Succinic acid	Sigma Aldrich	Cat#S3674-2506
DTT	RPI	Cat#D110000-25.0
Magnesium acetate	Sigma Aldrich	Cat#228648-500G
Glycerol	Fisher	Cat#633-4
GSH Sepharose beads	GE Healthcare	Cat#17-07560-04
IPTG	Gold Biotechnology	Cat#I24816100
EDTA	RPI	Cat#E57020-500.0
Tris hydroxymethyl aminomethane	RPI	Cat#T60040-5000.0
EGTA	RPI	Cat#E57060-100.0
Ni-NTA Agarose	QIAGEN	Cat#30320
Amylose resin	New England Biolabs	Cat#E8021L
Maltose	Sigma Aldrich	Cat#M5885-100G
Glutathione (reduced)	Sigma Aldrich	Cat#G4351-100G
Imidazole	Sigma Aldrich	Cat#92527-1KG
TEV Protease	This paper	N/A
RanGTP	Fung et al., 2015	N/A
M9M	Cansizoglu et al., 2007	N/A
^{15}N Ammonium Chloride	Cambridge Isotope Lab, Inc	Cat#NLM-467-1
Glucose (d7)	Cambridge Isotope Lab, Inc	Cat#DLM-2062-PK
2-Mercapto ethanol	Sigma Aldrich	Cat#M6250-100 ML
Leupetin	Sigma Aldrich	Cat#L2884
Benzamidine	Sigma Aldrich	Cat#B6506
Sodium Azide	Sigma Aldrich	Cat#S2002
Bis-TRIS	Sigma Aldrich	Cat#B9754
MES	Sigma Aldrich	Cat#M8250
PMSF	Sigma Aldrich	Cat#10837091001
Deuterium Oxide	Cambridge Isotope Lab, Inc	Cat#DLM-4-1000
Potassium Phosphate (monobasic)	ACROS Organics	Cat#AC205920025
Sodium Phospahte (dibasic)	Fisher	Cat#S375-212
Thiamin	Sigma Aldrich	Cat#S375-212
Magnesium Chloride	Fisher	Cat#M35-212
Calcium Chloride	Sigma Aldrich	Cat#449709
Antipain	Sigma Aldrich	Cat#0791
Superdex 200	GE Healthcare	Cat#28989336
Superdex 75	GE Healthcare	Cat#28989334
Source 15S	GE Healthcare	Cat#17094402
Source 15Q	GE Healthcare	Cat#17094702
Snap surface 649	New England BioLabs	Cat#S9159S
Kapβ2	Chook et al., 2002	N/A
Impα	This paper	N/A

(*Continued on next page*)

Continued

REAGENT or RESOURCE	SOURCE	IDENTIFIER
Kapβ2ΔLoop	Chook et al., 2002	N/A
Kap121	This paper	N/A
Impβ	This paper	N/A
6xHisMBP-FUS(Full length)	This paper	N/A
MBP-FUS(cNLS), Full length FUS with residues 501-526 replaced with PKKKRKV	This paper	N/A
MBP-FUS(NES), Full length FUS with residues 501-526 replaced with YSTVDEMTKKFGTLTIHD	This paper	N/A
MBP-FUS(IK-NLS), Full length FUS with residues 501-526 replaced with 140-SANKVTKNKSNSSPYLNKRRGKPGPDS-166 from Pho4	This paper	N/A
6xHisMBP-FUS(1-500)	This paper	N/A
6xHisMBP-FUS(1-452)	This paper	N/A
6xHisMBP-FUS(1-370)	This paper	N/A
6xHisMBP-FUS(Y5A), Full length FUS with mutations Y38A, Y41A, Y97A, Y100A, Y149A	This paper	N/A
MBP-FUS(RtoK), Full length FUS with all Arg residues in RGG1, RGG2 and RGG3 mutated to Lys	This paper	N/A
6xHisMBP-FUS(ΔRRM), Full length FUS with residues 286-370 removed	This paper	N/A
6xHisMBP-FUS(ΔZnF), Full length FUS with residues421-452 removed	This paper	N/A
MBP-FUS(1-163) or MBP-FUS LC	Burke et al., 2015	N/A
6xHisMBP-FUS(164-500)	This paper	N/A
6xHisMBP-FUS(164-526)	This paper	N/A
6xHisMBP-RGG1, FUS residues 164-267	This paper	N/A
6xHisMBP-RGG1-RRM, FUS residues 164-370	This paper	N/A
6xHisMBP-RRM, FUS residues 285-371	This paper	N/A
MBP-RGG2-ZnF, FUS residues 371-452	This paper	N/A
6xHisMBP-ZnF, FUS residues 415-460	This paper	N/A
6xHisMBP-ZnF-RGG3, FUS residues 421-500	This paper	N/A
MBP-FUS(371-526)	This paper	N/A
MBP-FUS(456-526)	This paper	N/A
Bacterial and Virus Strains		
Escherichia coli BL21(DE3)	New England Biolabs	Cat#C2527I
Recombinant DNA		
pGEX-TEV	Chook and Blobel, 1999	N/A
pMAL-TEV	Chook et al.,2002	N/A
p6xHisMAL-TEV	This paper	N/A
pTHMT	Burke et al., 2015	N/A
Oligonucleotides		
6FAM-prD	Integrated DNA Technologies	N/A
6FAM-TERRA	Integrated DNA Technologies	N/A
Deposited Data		
Kapβ2-FUS(Full Length) crystal structure	This paper	PDB: 5YVG
Kapβ2-FUS(371-526) crystal structure	This paper	PDB: 5YVH
Kapβ2-FUS(456-526) crystal structure	This paper	PDB: 5YVI

(*Continued on next page*)

Continued

REAGENT or RESOURCE	SOURCE	IDENTIFIER
Software and Algorithms		
NITPIC	Scheuermann and Brautigam, 2015	http://biophysics.swmed.edu/MBR/software.html
SEDPHAT	Brautigam et al., 2016	http://www.analyticalultracentrifugation.com/sedphat/
GUSSI	Brautigam, 2015	http://biophysics.swmed.edu/MBR/software.html
Coot	Emsley et al., 2010	http://www2.mrc-lmb.cam.ac.uk/personal/pemsley/coot/
PyMOL	Schrodinger	https://pymol.org/2/
Phenix	Adams et al., 2010	https://www.phenix-online.org/
phenix.refine	Afonine et al., 2012	https://www.phenix-online.org/
HKL3000	Minor et al., 2006	http://www.hkl-xray.com/
X-triage	Adams et al., 2010	https://www.phenix-online.org/
Molprobity	Chen et al., 2010	http://molprobity.biochem.duke.edu/
PHASER	Adams et al., 2010	https://www.phenix-online.org/
ATSAS package (DAMMIF/ DAMMIN/ DAMAVER/ PRIMUS), version 2.6	Petoukhov et al., 2012	https://www.embl-hamburg.de/biosaxs/software.html
SASTOOL, version 0.9.5.3	SSRL beamline 4-2 at SLAC	http://ssrl.slac.stanford.edu/~saxs/analysis/sastool.htm
SAXS MOW, version 1.0	SAXS beam line at the Brazilian Synchrotron Light National Laboratory	http://www.if.sc.usp.br/~saxs/obsolete/obsolete.html
GNUPLOT, version 4.8	Open software maintained by the developer community	http://www.gnuplot.info/
Adobe Illustrator	Adobe Illustrator® CC	https://www.adobe.com/
nmrPipe	Delaglio et al., 1995	https://www.ibbr.umd.edu/nmrpipe https://sbgrid.org/
Analysis	Vranken et al., 2005	https://www.ccpn.ac.uk/v2-software/software/analysis
Swiss-Model	Guex et al., 2009	https://swissmodel.expasy.org/

CONTACT FOR REAGENT AND RESOURCE SHARING

Further information and requests for resources and reagents should be directed to and will be fulfilled by the Lead Contact, Yuh Min Chook (yuhmin.chook@utsouthwestern.edu).

EXPERIMENTAL MODEL AND SUBJECT DETAILS

All recombinant proteins were expressed in BL21 (DE3) *E. coli* cells growing in LB medium or M9 medium.

METHOD DETAILS

Constructs, protein expression and purification

Kapβ2, Kapβ2Δloop (residues 337– 367 replaced with a GGSGGSG linker), Impα, Impβ, Kap121 and CRM1 were expressed as GST-fusions, which were generated by inserting PCR fragments of the gene of interest (all karyopherins, except the *S. cerevisiae* Kap121, are human proteins) into the pGEX-TEV plasmid, which is a pGEX4T3 vector (GE Healthcare, UK) modified to include a TEV cleavage site (Chook and Blobel, 1999). All FUS proteins were expressed from MBP-fusion constructs using the pMAL-TEV vector, which is a pMAL (New England BioLabs, Ipswich, MA) modified to contain a TEV cleavage site (Chook et al., 2002) or a pMAL-TEV vector modified to express His_6-MBP instead of MBP (p6xHisMal-TEV). FUS mutations were made by site-directed mutagenesis using a Quik-Change Site-Directed Mutagenesis Kit (Stratagene, La Jolla, CA), and all constructs were sequenced. MBP-FUS(cNLS), MBP-FUS(IK-NLS) and MBP-FUS(NES) chimeras were made by inverse PCR method. FUS residues 501-526 were replaced with either $SV40^{NLS}$ (PKKKRKV), Pho4 residues 140-166 (^{140}SANKVTKNKSNSSPYLNKRRGKPGPDS^{166}) or the NES from the NS2 protein

of the MVM virus (YSTVDEMTKKFGTLTIH), respectively. A MBP-FUS-SNAP construct was generated by cloning in a SNAP tag (New England BioLabs), preceded by a TGGGS linker, at the C terminus of MBP-FUS (full-length).

All recombinant proteins were expressed individually in BL21 (DE3) *E. coli* cells (induced with 0.5 mM isopropyl-β-d-1-thiogalactoside (IPTG) for 12 hours at 25°C for importins and at 18°C for FUS). Bacteria expressing importins were lysed with the EmulsiFlex-C5 cell homogenizer (Avestin, Ottawa, Canada) in buffer containing 50 mM Tris pH 7.5, 200 mM NaCl, 20% (v/v) glycerol, 2 mM DTT, 1 mM EDTA, and protease inhibitors. To purify untagged importins, GST-importins were first purified by affinity chromatography using GSH Sepharose beads (GE Healthcare, UK), eluted, cleaved with TEV protease, and further purified by ion-exchange and gel filtration chromatography in TB buffer (20 mM HEPES pH 7.4, 200 mM NaCl, 2 mM DTT, 2 mM $Mg(OAC)_2$, 10% glycerol, 1 mM EGTA). For pull-down binding assays, affinity purified GST-importins were eluted and then dialyzed against buffer containing 20 mM HEPES pH 7.4, 150 mM NaCl, 2 mM DTT and 10% glycerol.

Bacteria expressing MBP-FUS proteins for crystallization, turbidity, imaging and pull-down binding assays were lysed in 50 mM HEPES pH 7.4, 1.5 M NaCl, 10% glycerol, 2 mM DTT (high salt to disrupt association with nucleic acid). MBP-FUS proteins were purified by affinity chromatography using amylose resin (New England BioLabs, Ipswich, MA), eluted with buffer containing 20 mM HEPES pH 7.4, 150 mM NaCl, 2 mM DTT, 10% glycerol, and 20 mM maltose and either dialyzed extensively in final maltose-free buffers to remove maltose or further purified by ion-exchange chromatography. Purification of the MBP-FUS proteins always included either high salt or RNase A treatment to eliminate RNA (purified proteins have A_{260}/A_{280} ratios of 0.50-0.71), and the absence of EDTA to maintain the fold of its zinc finger domain. MBP-FUS proteins are also free of maltose since they are able to be immobilized on amylose resin.

RanGTP (GSP1 residues 1-179, Q71L) and M9M was purified as previously described (Cansizoglu et al., 2007; Fung et al., 2015). *E. coli* expressed His_6-RanGTP was purified using affinity and cation exchange chromatography. Purified protein was concentrated and exchanged buffer into 20 mM HEPES pH 7.4, 100 mM sodium chloride, 4 mM magnesium acetate, 1 mM DTT, 10% Glycerol. cNLS, M9M and IK-NLS peptides were expressed as a GST-fusions, purified using GSH Sepharose followed by cleavage of GST tag and further purified by gel filtration in buffer containing 20 mM HEPES pH 7.4, 150 mM NaCl, 2 mM DTT and 10% glycerol.

Turbidity Assays

FUS turbidity analysis at room temperature

Importins and its NLSs, M9M or buffer are mixed at room temperature for 30 minutes prior to turbidity assays. 8 μM MBP-FUS and buffer, 8 μM importins (importins, importin•NLS or Kapβ2•M9M) ± 8 μM RanGTP were mixed in buffer containing 20 mM HEPES pH 7.4, 150 mM NaCl, 2 mM DTT, 2 mM $Mg(OAC)_2$, 10% glycerol to reaction volumes of 100 μL. TEV was added at time = 0 min to final concentration of 25 μg/mL. Absorbance at 395 nm (OD_{395nm}) was monitored at room temperature using Variskan plate reader (Thermo Fisher Scientific, Inc.).

Temperature dependent FUS turbidity analysis

Prior to tracking turbidity, 8 μM MBP-FUS proteins (in buffer containing 20 mM HEPES pH 7.4, 150 mM NaCl, 2 mM DTT, 2 mM magnesium acetate, 10% glycerol) were treated with Tev protease (final concentration 25 ug/mL Tev) in reaction volumes of 500 uL for 3 hours at room temperature, and then placed in a cuvette. OD_{395nm} was measured using a Cary 100 UV-Visible spectrophotometer equipped with a Peltier thermal controller (Agilent Technologies, Australia). FUS reaction mixtures in cuvettes were held at 45°C or 40°C for 10 min then cooled gradually at a rate of −0.5°C/min. OD_{395nm} of FUS proteins were monitored every 0.5°C. T_{Cloud} is the x-intercept of tangent at inflection point of the curve (mean of 3 technical replicates, ± SD).

Monitoring interactions between Importins and FUS

In vitro pull-down binding assays were performed using GST-Kapβ2, GST-Impα, GST-Impα/β or GST-Kap121 immobilized on GSH Sepharose beads. ~4 μM GST-importins were immobilized on beads. 30 μL of GST-importins beads are incubated with 8 μM MBP-FUS proteins (total 80 μg) for 30 min at room temperature and washed three times with buffer containing 20 mM HEPES pH7.4, 150 mM NaCl, 10% glycerol, 2 mM $Mg(OAC)_2$ and 2 mM DTT. Bound proteins were separated by SDS-PAGE and stained with Coomassie blue.

Gel filtration chromatography to assess complex formation was performed using a Superdex 200 10/300 GL column (GE Healthcare). 500 μL of protein samples were loaded onto the column and eluted with buffer containing 20 mM HEPES pH7.4, 150 mM NaCl, 10% glycerol, 2 mM $Mg(OAC)_2$ and 2 mM DTT. Eluted fractions were visualized by SDS-PAGE/Coomassie Blue.

Binding affinities of MBP-FUS proteins to Kapβ2 were measured using isothermal titration calorimetry (ITC). ITC experiments were performed with a Malvern iTC200 calorimeter (Malvern Instruments, Worcestershire, UK). Proteins were dialyzed overnight against buffer containing 20 mM HEPES pH 7.4, 150 mM NaCl, 10% glycerol, and 2 mM β-mercaptoethanol. 50-100 μM MBP-FUS proteins were titrated into the sample cell containing 5–10 μM recombinant Kapβ2. ITC experiments were performed at 20°C with 19 rounds of 2 μL injections. Data were integrated using NITPIC (Scheuermann and Brautigam, 2015), globally fitted using SEDPHAT (Brautigam et al., 2016; Zhao et al., 2015), and plotted with GUSSI (Brautigam, 2015). Confidence intervals for reported K_Ds were calculated with projection method at 68.3% confidence level in SEDPHAT.

Monitoring the effects of Kapβ2 on FUS-RNA interactions

prD (5′-AUUGAGGAGCAGCAGAGAAGUUGGAGUGAAGGCAGAGAGGGGUUAAGG-3′, 48-mer) and TERRA (5′-UUAGGGUUAG GGUUAGGGUUAGGG-3′, 24-mer) were chemically synthesized (Integrated DNA Technologies, Coralville, IA). Both RNAs were 5′ end labeled with 6-FAM (Fluorescein). prD (in buffer containing 20 mM HEPES pH 7.4, 150 mM KCl, 2 mM DTT, 2 mM magnesium acetate, 10% glycerol) was heated at 95°C for 5 min and snap-cooled on ice for 10 min. TERRA in the same buffer was heated at 95°C for 5 min and cooled down to 4°C at a rate of 1°C/min for annealing on T100 thermal cycler (Bio-Rad, Hercules, CA). RNA, MBP-FUS and Kapβ2 were mixed at room temperature for at least 10 min prior to gel filtration chromatography. 1 μM prD or 2 μM TERRA ± 3 μM MBP-FUS ± 3.2 μM Kapβ2 were mixed in buffer containing 20 mM HEPES pH 7.4, 150 mM KCl, 2 mM magnesium acetate, 10% glycerol and 2 mM DTT. Gel filtration chromatography with a Superdex 200 10/300 GL column (GE Healthcare) was used to assess complex formation. 100 μL of proteins ± RNA samples were loaded onto the column and eluted with buffer containing 20 mM HEPES pH7.4, 150 mM KCl, 10% glycerol, 2 mM magnesium acetate and 2 mM DTT. Protein(s) in eluted fractions (500 μL each) were visualized by SDS-PAGE/Coomassie Blue. The RNA in each fraction was tracked by monitoring fluorescence emission at 520 nm from the 6-FAM tag (excited at 495 nm) using Varioskan plate reader (Thermo Fisher Scientific, Inc.).

Imaging of turbid FUS solution

For imaging experiments, purified MBP-FUS-SNAP was labeled with SNAP-Surface 649 fluorophore (New England BioLabs) by incubating with 5-fold excess fluorophore for 2 hours at room temperature. Unreacted fluorophore was removed by dialysis. 5 μM MBP-FUS, 0.5 μM MBP-FUS-SNAP$^{\text{SNAP-Surface 649}}$ and either buffer or 10 μM Kapβ2 ± 15 μM M9M or 15 μM RanGTP were mixed at room temperature in total volumes of 100 μL in individual wells of CultureWell non-removable chamber cover glass (Grace Bio-Labs). All wells were made up to 100 μL with buffer containing 10 mM HEPES pH7.4, 150 mM NaCl, 2 mM $Mg(OAC)_2$, 2 mM DTT and 10% glycerol. Tev protease was added to final concentration of 1.5 μM at time = 0 hr. Wells containing protein mixtures were imaged by spinning disk confocal microscopy beginning at time = 1 hr. Spinning disk confocal microscopy was executed using a Yokogawa CSU-X scanhead (Solamere Technology Group) mounted on an ASI Rapid Automated Modular Microscope system equipped with motorized XT stage and piezo z-motor in the stage (ASI), an Andor iXon Ultra 897 camera (Andor), and laser illumination using a VersaLase laser system equipped with 405, 488, 561, and 640 nm laser (Vortran Laser Technology). A multi-bandpass dichroic mirror in the Yokogawa scanhead was combined with dye specific emission filters (Chroma Technology Corp.) in a Finger Lakes Instrument filter wheel (Finger Lakes Instrument). Nikon 60x 1.4na oil immersion objective lens (Nikon) was used. The microscope system was operated using the Micro-Manager software package (https://micro-manager.org).

Polarized light microscopy was performed with the LC-PolScope, employing a liquid crystal based universal compensator to generate retardance maps that are independent of the orientation of the slow axis of birefringence (Oldenbourg, 1991; Oldenbourg and Mei, 1995). The instrument was implemented on an inverted microscope stand (Nikon Eclipse Ti-E), equipped with 60x/1.4 NA objective and condenser lens of matching NA, 546/12 nm interference filter, liquid crystal device, polarization components, and processing software as described and available from http://OpenPolScope.org.

To perform temperature-dependent FUS studies by fluorescence microscopy, mixtures of 2 μM MBP-FUS wt (MBP-FUS(1-452), or MBP-FUS(ΔRRM)), 20 nM FUS-GFP (gift from Avinash Patel and Tony Hyman) and Tev protease were loaded onto a CherryTemp™ heater/cooler stage (Cherry BioTech). The FUS mixtures were treated with Tev protease at room temperature for 50 min to form phase-separated FUS droplets. The phase separated mixtures were cooled using the CherryTemp™ temperature controller to either 10°C or 15°C, held at those temperatures for 2 min, and then increased by 2°C increments to a maximum temperature of 43°C or 44°C. The sample was held at each temperature for 2-3 min prior to acquisition of a 50 μm Z stack (1 μm increments) using spinning disk confocal microscopy. Maximum projection images from the Z stack 10-50 μm above the slide surface were generated. To calculate T_{cloud}, images in this same portion of the Z stack were segmented using the Triangle algorithm in ImageJ and the total number of FUS droplets was determined after a filter for circularity (> 0.5) and size (> 0.5 μm^2). T_{cloud} was determined from the x-intercept of a line fit to the first six (wt and FUS(1-452)) or eight (FUS(ΔRRM)) points in the (number of puncta) versus temperature curve.

Dynamic light scattering analysis

Dynamic light scattering (DLS) was performed to examine polydispersity of MBP-FUS alone and the MBP-FUS•Kapβ2 complex. We used a DynPro DLS instrument (Wyatt Technology). Samples of 12 μM MBP-FUS ± 12 μM Kapβ2 in buffer containing 10 mM HEPES pH7.4, 150 mM NaCl, 10% glycerol and 2 mM 2-mercaptoethanol were loaded into the cuvette. Scattered light intensity at 25°C was analyzed using the software SEDPHAT.

To investigate whether Kapβ2 has attractive or repulsive self-interactions, we determined its diffusion coefficient at different protein concentrations, also using DLS. Prior to the experiment, Kapβ2 (in buffer containing 150 mM NaCl, 20 mM HEPES pH 7.5, 2 mM $Mg(OAc)_2$, 2 mM DTT, 10% glycerol) was centrifuged at 16,000 x g for 10 min and filtered through an ultrafree-MC GV centrifugal filter with a 0.22 μm pore size (EMD Millipore). Measurements were performed at 25 degree on a DynaPro DLS instrument (Wyatt Technology). The scattering intensities were averaged over twenty runs, each with a 20 s acquisition time. The diffusion coefficients were analyzed using Dynamics software (Wyatt Technology). Molecules with attractive interactions form larger species that diffuse more slowly as concentration increases; conversely, molecules with repulsive interactions do not self-associate, and diffuse more

rapidly at higher concentrations interactions. The concentration dependence of diffusion coefficient (D) can be described approximately by $D = D_0 (1 + \kappa_D c)$, where D_0 is the diffusion coefficient at infinite dilution, c is the protein concentration and κ_D is the diffusion interaction parameter. A positive κ_D suggests net repulsive interactions and a negative κ_D indicates net attractive interactions (Connolly et al., 2012).

NMR analysis of FUS LC with Kapβ2

^{15}N-FUS LC (residues 1-163) was expressed by growing *E. coli* BL21 Star (DE3) in M9 minimal medium with $^{15}NH_4Cl$. ^{15}N-FUS LC was purified from inclusion bodies by resolubilizing in buffer containing 8M urea followed by HisTrap affinity chromatography and cleavage with TEV protease. The eluted protein was exchanged and concentrated into 20 mM CAPS pH 11.0 (no denaturant). To make samples for NMR, concentrated FUS LC was diluted into 20 mM MES/Bis-Tris (pH 6.6), 150 mM NaCl, 2 mM DTT, 10% glycerol and 0.01% NaN_3, followed by addition of 10% v/v D_2O. Samples with FUS LC and Kapβ2 variants were made identically, with Kapβ2 present in the MES/Bis-Tris buffer before addition of FUS LC. Independent samples were made for each Kapβ2 concentration.

NMR data for ^{15}N-labeled FUS LC were acquired at 10°C and 25°C on a Bruker 850 MHz spectrometer equipped with 5 mm cryogenically cooled triple- resonance pulsed field gradient (TCI) probe. Two-dimensional (2D) $^1H-^{15}N$ HSQC spectra were collected with spectral widths of 8928.6 Hz and 1723.5 Hz with 1536 and 256 complex data pairs in the ^{1}H and ^{15}N dimensions, respectively. An inter-scan delay of 1 s was employed between successive transients. States-TPPI was employed for frequency discrimination in the indirectly detected dimension. Reference HSQC spectrum (without Kapβ2) was acquired on ^{15}N-labeled FUS LC (75 μM). To probe interactions between FUS LC and Kapβ2 or Kapβ2-FUS PY-NLS, 100 μM of unlabeled Kapβ2 or Kapβ2 bound to FUS PY-NLS (purified by size exclusion in presence of excess FUS PY-NLS and then exchanged by centrifugal filtration into NMR buffer) was added to the ^{15}N-labeled FUS LC in the stated ratios. Importantly, titrations were performed by generating a series of independent matched samples. All spectra were recorded in 5 mm NMR tubes and sample volume was always maintained to 500 μL in 90%H_2O/10%D_2O.

NMR analysis of FUS(164-526), FUS(164-500) and smaller FUS fragments with Kapβ2

Preparation of ^{15}N-labeled FUS(164-526), FUS(164-500) and RGG2-ZnF

^{15}N-labeled His_6-MBP-FUS(164-526), MBP-FUS(164-500) and MBP-RGG2-ZnF (FUS residues 371-452) were expressed by growing BL21(DE3) cells harboring the respective plasmids in M9 minimal medium with $^{15}NH_4Cl$ as a sole source of nitrogen. Protein expression was induced with 1 mM IPTG, at 16°C for 18 hours. Harvested cells were lyzed in buffer containing 20 mM Na-Phosphate buffer (pH 6.5), 1.5 M NaCl, 1 mM PMSF, 5 mM 2-mercaptoethanol (BME), 1μg/ml Leupeptin, 1 mM Benzamidine 1 μg/ml Antipain, and 10% Glycerol using EmulsiFlex-C5 (Avestin, Ottawa, Canada). ^{15}N-MBP-FUS(164-500) was purified by affinity chromatography using Amylose beads (washed extensively, first with buffer containing 20 mM Na-Phosphate pH 6.5, 1.5 M NaCl, 5 mM BME and then with the same buffer containing 1 M NaCl). On-bead TEV reaction was performed to remove MBP tag, and cleaved ^{15}N-FUS(164-500) was collected as flow-through and was dialyzed against buffer containing 20 mM HEPES (pH 7.4), 150 mM NaCl, 2 mM BME. The protein was further purified by cation exchange chromatography (Source 15S, GE healthcare life sciences). Fractions of clean FUS(164-500) were pooled and concentrated to 10 ml. NaCl concentration in the FUS(164-500) solution was then raised to 1M followed by gel filtration chromatography (Superdex 200 HiLoad 26/600) in buffer containing 20 mM HEPES (pH 7.4), 1 M NaCl, 2 mM BME. ^{15}N-labeled FUS(164-500) elutes as a peak corresponding to monomeric molecular weight. Finally, ^{15}N-labeled FUS(164-500) was dialyzed against NMR buffer containing 20 mM Bis-Tris/MES (pH 6.5), 150 mM NaCl, 2 mM DTT, 10% glycerol, 1 mM NaN3. ^{15}N-MBP-RGG2-ZnF was purified similarly, except the gel filtration step was omitted. ^{15}N-FUS(164-526) was purified as ^{15}N-FUS(164-500) except the former was purified using Ni-NTA instead of amylose affinity chromatography.

Preparation of ^{2}H/^{15}N/^{12}C-labeled FUS(164-500)

Deuterated ^{15}N-labeled MBP-FUS(164-500) was expressed by growing BL21(DE3) cells harboring plasmids for MBP-FUS(164-500) in modified M9+ medium in 100% D_2O (99% ^2H_2O, Cambridge isotope limited, inc) with $^{15}NH_4Cl$ and ^{12}C glucose-d6 (Cambridge isotope limited, inc) as sole source of nitrogen and carbon, respectively. The starter culture was prepared by inoculating 1 mL of LB with a single colony of freshly transformed BL21 cells. Cells were allowed to grow at 37°C till OD_{600} reached 0.8 (~3 hr). 400 μl of the previous culture was used to inoculate 10 mL of LB prepared in 100% D_2O and subsequently 10 mL of LB/D_2O (OD_{600} 0.8) culture was used to inoculate 100 mL of medium M9+ medium. Cells were grown at 37°C until OD_{600} reached ~4, and the whole culture was used to inoculate 1000 mL of M9+/D_2O and grown at 37°C until OD_{600} reached 3.0. Protein expression was then induced with 0.8 mM IPTG, at 25°C for 30 hours. Harvested cells were lyzed and the protein purified as described for ^{15}N-labeled FUS(164-500) preparation except that final NMR buffer was 20 mM phosphate buffer (pH 6.5), 150 mM NaCl, 2mM DTT, 10% glycerol and 1 mM NaN_3.

Preparation of ^{15}N-labeled RGG1, RGG1-RRM, RRM, ZnF and ZnF-RGG3

^{15}N-labeled His_6-MBP-RGG1 (FUS residues 164-267), His_6-MBP-RGG1-RRM (FUS residues 164-370), His_6-MBP-RRM (FUS residues 285-371), His_6-MBP-ZnF (FUS residues 415-460) and His_6-MBP-ZnF-RGG3 (FUS residues 421-500) proteins were expressed using the same protocol as protonated ^{15}N-labeled MBP-FUS(164-500). Cells were lysed in buffer containing 50 mM Tris pH 8.0, 10 mM Imidazole pH 7.5, 5 mM BME, 1 M NaCl, 1mM PMSF, 10% Glycerol, 1μg/ml Leupeptin, 1 mM Benzamidine, 1μg/ml Antipain.

^{15}N-labeled His$_6$-MBP-RGG1 and His$_6$-MBP-ZnF-RGG3 proteins were first purified on Ni-NTA beads (washed extensively buffer containing 50 mM Tris pH 8.0, 10 mM Imidazole pH7.5, 1 mM BME, 1.5 M NaCl, followed by second wash with buffer containing 50 mM TRIS pH 8.0, 25 mM Imidazole pH 7.5, 1 mM BME and 200 mM NaCl). Bound material was eluted with buffer containing 50 mM Tris pH 8.0, 500 mM Imidazole (pH 7.5) 1 mM BME, 200 mM NaCl, and TEV was added to eluted materials for cleavage at 4°C. Cleaved ^{15}N-labeled FUS fragments were further purified by cation exchange chromatography (Source 15S, GE healthcare life sciences), and pure proteins were then dialyzed against NMR buffer 20 mM Bis-Tris/MES pH 6.5, 150 mM NaCl, 2 mM DTT, 10% glycerol and 1 mM NaN3. ^{15}N-labeled RGG1-RRM was purified similarly except an additional final gel filtration (SD 75) step. His$_6$-MBP-RRM and His$_6$-MBP-ZnF were purified similarly except gel filtration (SD 75 or SD peptide 10/300, respectively) was substituted for cation exchange chromatography.

Cross saturation transfer experiment

In order to identify the interfaces between FUS(164-500) and Kapβ2•M9M, cross-saturation experiment was performed on an Agilent 800 MHz spectrometer equipped with a 5 mm cryogenically cooled triple-resonance pulsed field gradient (TRPFG) probe. Perdeuterated ^{2}H/^{15}N-labeled FUS(164-500) (28 μM) was mixed with 42 μM of unlabeled Kapβ2•M9M in 90% H_2O/D_2O. Cross saturation of ^{2}H/^{15}N FUS was achieved by saturating aliphatic protons of Kapβ2•M9M for 1.5 s. A train of CHIRP adiabatic pulses with RF amplitude of 125 Hz, excitation centered at 2 ppm, which provided a 2400 Hz irradiation bandwidth, was used for saturation, followed by acquisition of ^{1}H-^{15}N TROSY (Pervushin et al., 1997) HSQC with an intertransient delay 2 s. A reference spectrum was acquired with the same experimental setup, except that center of CHIRP pulse train was shifted to ~50000 Hz off resonance (no saturation). Intensity of cross-peaks in irridiated (I, with saturation) and reference (I_0, no saturation) spectra were calculated by using nmrPipe (Delaglio et al., 1995) and Analysis module in CCPN (Vranken et al., 2005).

Line broadening experiments

NMR data for ^{15}N-labeled FUS(164-500) were acquired at 25°C on an Agilent 600 MHz spectrometer equipped with a 5 mm cryogenically cooled triple- resonance pulsed field gradient (TRPFG) probe. The sample temperature was maintained at 25°C during all experiments. Two-dimensional (2D) ^{1}H−^{15}N HSQC spectra were collected with spectral widths of 8000 Hz and 1920 Hz and acquisition times of 64 ms and 67 ms in the ^{1}H and ^{15}N dimensions, respectively. An inter-scan delay of 1 s was employed between successive transients. Rance-Kay mode of quadrature detection was employed for frequency discrimination in the indirectly detected dimension. Reference HSQC spectrum (without Kapβ2•FUS PY-NLS or Kapβ2•M9M) was acquired for 17 μM ^{15}N-labeled FUS(164-500). To probe interactions between FUS(164-500) and Kapβ2, 17 μM ^{15}N-FUS(164-500) was titrated with varying concentrations of unlabeled Kapβ2•FUS PY-NYLS (FUS(164-500):Kapβ2•FUS PY-NLS in molar ratios of 1:0.5, 1:1 and 1:2) and with unlabeled Kapβ2•M9M (FUS(164-500):Kapβ2•M9M molar ratio of 1:3). All spectra were recorded in a 5 mm NMR tubes and samples always maintained to 300 μL in 90%H_2O/10%D_2O. Each titration experiment was performed on a freshly prepared sample to avoid a dilution effect upon addition of the Kapβ2 complex.

NMR data for ^{15}N-FUS(164-526) were acquired similarly. To probe the interaction between FUS(164-526) and Kapβ2, ^{1}H-^{15}N spectra of 15 μM ^{15}N-FUS(164-526) were acquired in presence of 15 μM Kapβ2. A reference spectrum was acquired with 15 μM ^{15}N FUS (164-526) alone.

Interaction between FUS fragments and Kapβ2·M9M

In order to probe interaction between FUS fragments (RGG1, RGG1-RRM, RGG2-ZnF, ZnF-RGG3) and Kapβ2•M9M, different fragments (50 μM of each fragment) were titrated with Kapβ2•M9M (100 μM) in a 5 mm shigemi NMR tube. 2D ^{1}H-^{15}N HSQC spectra were acquired on an Agilent 600 MHz spectrometer equipped with a 5 mm cryogenically cooled triple- resonance pulsed field gradient (TRPFG) probe. All data were acquired at 25°C in 90% H_2O/10% D_2O. Spectra were collected with sweep widths 8000 Hz and 1920 Hz and acquisition times of 64 ms and 67 ms in the ^{1}H and ^{15}N dimensions, respectively. An inter-transient delay of 1 s was employed between successive transients. Rance-Kay mode of quadrature detection was employed for frequency discrimination in the indirectly detected dimension. A reference experiment was acquired for each fragment (at 50 uM concentration) without Kapβ2•M9M, with the same experimental setup. Cross-peak intensities in absence (I_0) and presence (I) of Kapβ2•M9M were measured by using nmrPipe and Analysis module in CCPN.

All NMR data were processed using NMRPipe/NMRDraw processing software. Directly and indirectly detected time domain data were processed by applying a 90° phase-shifted squared sine bell or sine bell, respectively. Zero-filling was employed prior to Fourier transformation. Processed data were analyzed using the ipap.com script distributed with nmrPipe. The intensity of a resonance in the control experiment was taken as the reference intensity (I_0). The decrease in intensity (I) due to the line broadening and/or chemical exchange contribution to the relaxation, arising from interaction between ^{15}N-labeled FUS and Kapβ2 complex was determined by measuring peak volume/height. A ratio of I/I_0 as a function of residue number/peak number was plotted to assess the interacting residues on FUS.

Homology modeling was used to construct a model of the FUS zinc finger. A sequence similarity search of FUS zinc finger against sequences in the PDB performed on using BLAST (https://blast.ncbi.nlm.nih.gov/Blast.cgi?PAGE=Proteins) identified PDB: 2K1P as the closest homolog (50% sequence identity). The homology model of the FUS zinc finger was built using SWISS-MODEL (Guex et al., 2009).

Small-angle X-ray scattering (SAXS)

SAXS experiments of MBP, MBP-FUS, Kapβ2, Kapβ2•FUS, and Kapβ2•MBP-FUS were carried out at Beamline 4-2 of the Stanford Synchrotron Radiation Lightsource (SSRL) in the SLAC National Accelerator Laboratory. At SSRL, the beam energy and current were 11 keV and 500 mA, respectively. A silver behenate sample was used to calibrate the q-range and detector distance. Data collection was controlled with Blu-Ice (Kim et al., 2014). We used an automatic sample delivery system equipped with a 1.5 mm-diameter thin-wall quartz capillary within which a sample aliquot was oscillated in the X-ray beam to minimize radiation damage (Kim et al., 2014). The sample was placed at 1.7 m from a MX225-HE (Rayonix, USA) CCD detector with a binned pixel size of 292 by 292 μm.

The SAXS profiles were collected at concentrations ranging from 0.5 either to 19.2 (Kapβ2) or up to 5.0 (all others) mg/mL. All protein samples were expressed and purified (as described above in Methods) in the protein storage buffers (10 mM HEPES pH 7.4, 150 mM NaCl, 20% glycerol, 2 mM $Mg(OAc)_2$, and 2 mM DTT for Kapβ2, 10 mM HEPES pH 7.4, 150 mM NaCl, 20% glycerol, 2 mM DTT, and protease inhibitors for Kapβ2-FUS, and 50 mM HEPES pH 7.4, 500 mM NaCl, 20% glycerol, 2 mM DTT, and protease inhibitors for all others). The 20% glycerol in the protein storage buffer protects the protein samples from radiation damage during X-ray exposure (Kim et al., 2014). To assess the potential effects of high glycerol concentration on the solution behavior of the proteins, we also collected SAXS profiles for all samples in buffer with 5% glycerol. No significant change in behavior was observed (Figure S7G); thus glycerol does not affect protein compaction in its low concentration ranging 5 to 20%. All solutions were filtered through 0.1 μm membranes (Millipore) to remove any aggregates. Up to 20 one-second exposures were used for each sample and buffer maintained at 15°C. Each of the resulting diffraction images was scaled using the transmitted beam intensity, azimuthally integrated by SASTool (http://ssrl.slac.stanford.edu/~saxs/analysis/sastool.htm) and averaged to obtain fully processed data in the form of intensity versus q [$q = 4\pi\sin(\theta)/\lambda$, θ = one-half of the scattering angle; λ = X-ray wavelength]. The buffer SAXS profile was subtracted from a protein SAXS profile. Subsequently, the mean of the lower concentration (0.5 - 1.0 mg/mL) profiles in the smaller scattering angle region ($q < 0.15$ A^{-1}) and the mean of the higher concentration (1.5 - 5.0 or higher mg/mL) profiles in the wider scattering angle region ($q > 0.12$ A^{-1}) were merged to obtain the final experimental SAXS profiles that are free of the concentration-dependent aggregation or polydispersity effect (Kikhney and Svergun, 2015).

The merged SAXS profiles were initially analyzed using the ATSAS package (Franke et al., 2017) to calculate radius of gyration (R_g^{SAXS}), maximum particle size (D_{max}), and pair distribution function (P(r)) (Figures 6E and S6; Table S4). The molecular weight (MW_{SAXS}) of each SAXS sample was estimated using SAXS MOW (Fischer et al., 2010) with a threshold of q_{max} = 0.2 - 0.3 $Å^{-1}$ (Table S4). The *ab initio* shape of the corresponding protein (Figure S7; transparent envelope) was computed from the experimental SAXS profile by running DAMMIF 20 times, and then refined through additional 50 DAMMIN runs followed by superposition and averaging with DAMAVER (Franke et al., 2017).

X-ray crystallography of Kapβ2·FUS complexes

To assemble and purify Kapβ2•FUS complexes for crystallization, bacteria expressing GST-Kapβ2Δloop and MBP-FUS were mixed and lysed together. Kapβ2•FUS complex was purified by tandem affinity chromatography using GSH Sepharose beads and amylose resin, cleaved with TEV protease, and purified by gel filtration chromatography in buffer containing 20 mM HEPES, pH 7.4, 110 mM potassium acetate, 2 mM DTT, 2 mM magnesium acetate, 1 mM EGTA and 20% glycerol. Kapβ2•FUS complexes were concentrated to 10 mg/mL for crystallization.

All Kapβ2•FUS crystals were obtained by hanging drop vapor diffusion at 20°C (1.0 μL protein + 1.0 μL reservoir solution) with reservoir solution of 0.8 M Succinic acid pH 7.0. Crystals were cryo-protected by addition of ~25% glycerol, and flash-cooled by immersion in liquid nitrogen. 0.9795Å wavelength X-ray diffraction data were collected at the Advance Photon Source 19ID beamline in the Structural Biology Center at Argonne National Laboratory. Diffraction data was indexed, integrated, and scaled using HKL3000 (Minor et al., 2006). The structure was determined by molecular replacement using PHASER with a search model of human Kapβ2 (Chain A from PDB ID 4FDD) (Cansizoglu and Chook, 2007). Several rounds of refinement using PHENIX and manual model building with Coot were performed (Adams et al., 2010; Emsley et al., 2010). X-triage analysis of the dataset for KapB2•full-length FUS indicated pseudo-merohedral twinning (Adams et al., 2010). Therefore the data was refined in phenix.refine with twin law l,-k,h, and twin fraction was refined to 36% (Afonine et al., 2012). FUS residues were built into the electron density maps at the last stages of the refinement. Final models of Kapβ2•FUS complexes show excellent stereochemical parameters based on Molprobity suite in PHENIX (Chen et al., 2010). Illustrations were prepared with PyMOL (Schrodinger, 2015). Kicked OMIT maps are calculated with PHENIX by omitting FUS.

QUANTIFICATION AND STATISTICAL ANALYSIS

Turbidity analyses in Figures 1B–1D, 2A–2C, 5A–5C, and S1E were each repeated three times. Standard deviation error bars were obtained from three technical replicates.

X-ray diffraction data was indexed, integrated and scaled using software HKL3000. Completeness, R_{merge}, $I/\sigma I$ and CC1/2 values were used to evaluate data. R_{work} and R_{free} were used to evaluate PHENIX-refined models, which were validated using the Molprobity suite in PHENIX.

ITC data in Figures S1B, S2B, and S2C, collected in triplicates using the MicroCal iTC$_{200}$ software. Individual thermograms were integrated and processed into binding isotherms using the NITPIC software. Analysis by NITPIC produces error of each titration, the incompentency of Kapβ2 and the binding isotherms. Triplicate isotherms are then populated into the SEDPHAT software for global fitting. A rigorous statistical analysis of the best fit is carried out using F-statistics. The triplicate datasets are then presented using GUSSI.

NMR analysis: Error in resonance intensity measurements reported in Figures 3, 4, 5, S3, and S5 were calculated by measuring signal-to-nosie ratio.

DATA AND SOFTWARE AVAILABILITY

The accession numbers for the crystal structures of Kapβ2•FUS(full-length), Kapβ2•FUS(371-526), and Kapβ2•FUS(456-526) reported in this paper are PDB: 5YVG, 5YVH, and 5YVI, respectively.

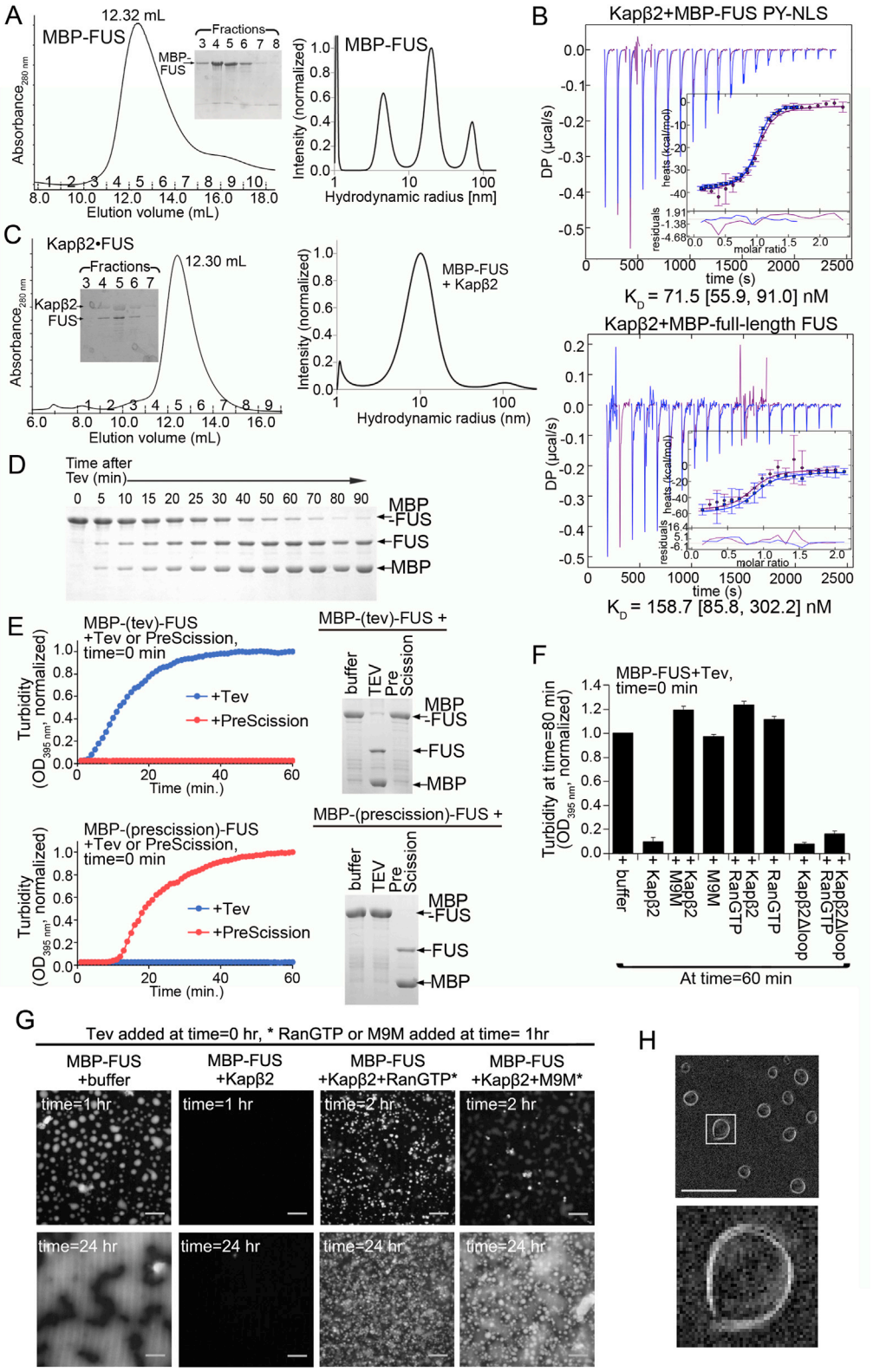

Figure S1. Solution Behavior of FUS Complexes and Microscopy of FUS LLPS, Related to Figure 1

(A) MBP-FUS is monomeric in size exclusion chromatography (left) but dynamic light scattering (DLS) analysis of 12 μM MBP-FUS shows polydispersity and presence of possibly very large MBP-FUS oligomers (right).

(legend continued on next page)

(B) Dissociation constants (K_Ds) of Kapβ2 binding to MBP-FUS PY-NLS (upper) and MBP-full length FUS (lower) by isothermal titration calorimetry at 20°C. In the upper panel, 50 μM Kapβ2 was titrated into 4.5 or 6.5 μM MBP-FUS PYNLS (residues 475-526). In the lower panel, 50 μM Kapβ2 was titrated into 4.5 or 5 μM MBP-full length FUS. Thermograms, binding isotherms and data fit residuals of two independent ITC experiments are plotted. KDs, obtained from NITPIC (integration software that estimates baseline error from individual isotherm data points) and SEDPHAT (performs global fitting of independent ITC experiments), are reported with 68.3% confidence interval in brackets. In the experiment of Kapβ2 binding to MBP-FUS PY-NLS, 2.3% of the MBP-FUS PY-NLS was incompetent. In the experiment of Kapβ2 binding to MBP-FUS, 8.6% of the MBP-FUS was incompetent.

(C) A purified Kapβ2•FUS complex is heterodimeric in size exclusion chromatography (left). DLS (right) shows Kapβ2 drastically reducing the MBP-FUS poly-dispersity and the majority of the Kapβ2•MBP-FUS complex behaves as a single species.

(D) Time course of Tev protease (added at time = 0 min) cleaving MBP from MBP-FUS at room temperature. Proteins were visualized by Coomassie blue stained SDS/PAGE.

(E) Turbidity (OD_{395nm}) of 8 μM MBP-FUS proteins with either a TEV protease ceavage site or a PreScission protease cleavage site between MBP and FUS. Turbidity was measured for 60 min at room temperature after Tev or PreScission treatment. Cleavage MBP-FUS by the proteases was visualized by Coomassie blue stained SDS/PAGE.

(F) Already turbid FUS (8 μM MBP-FUS treated with Tev for 60 min) were treated with either buffer, 8 μM Kapβ2 ± RanGTP or inhibitor M9M, or Kapβ2Δloop ± RanGTP at time = 60 min. Turbidity measurements 20 min later, at time = 80 min are shown (mean of 3 technical replicates, ± SD).

(G) Mixtures containing 5 μM MBP-FUS, 0.5 μM MBP-FUS-SNAP$^{SNAP\text{-}Surface\ 649}$ and either buffer or 10 μM Kapβ2 were treated with Tev protease (time = 0 hr) and imaged with spinning disk confocal microscopy 1 hr after later. By time = 1 hr, FUS has phase separated into liquid droplets that coalesce into large mats of phase separated protein by time = 24 hr. Kapβ2 prevents FUS phase separation, but this effect is reversed if either 15 μM RanGTP or 15 μM Kapβ2 inhibitor M9M is added. *RanGTP or M9M was added to the FUS+Kapβ2 mixture at time = 1 hr and imaged either 1 hr later (time = 2 hr) or at time = 24 hr. Images were obtained with spinning disk confocal microscopy (561 nm laser illumination; 60x 1.4na oil immersion objective lenses). 20 μm length scale bars are shown on the bottom right of all images.

(H) Polarized light microscopy of droplets (5 μM MBP-FUS+0.5 μM MBP-FUS-SNAP$^{SNAP\text{-}Surface\ 649}$, 1-2 hr of Tev treatment). Retardance images were recorded with the LC-PolScope - white corresponds to 2.5 nm retardance. The edge of each droplet is decorated with a birefringent double layer, an optical effect that stems from the refractive index difference between droplet and surrounding medium. The droplets display higher refraction than the medium, probably due to a higher protein/nucleotide concentration. The right panel, an enlarged droplet shows the lack of detectable birefringence in the interior of the droplet. The inside of each droplet has the same level of anisotropy as the surrounding medium, both of which are caused by the shot noise (photon statistics noise) inherent in the recorded image intensities. There is no order that we can detect in the interior of the droplets.

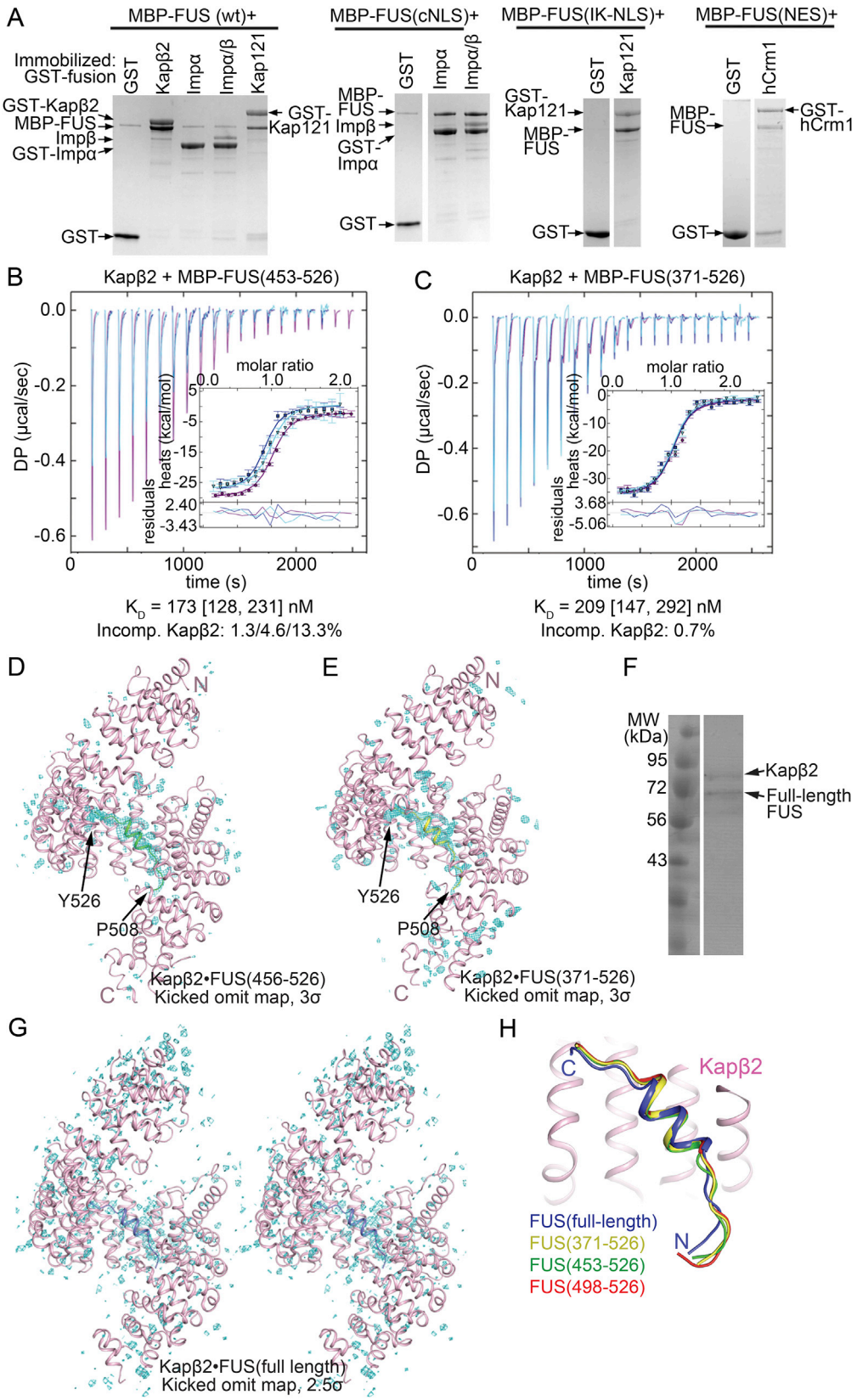

(legend on next page)

Figure S2. Interactions of MBP-FUS Chimeras with Importins, ITC and Crystal Structures of Kapβ2 Bound to FUS, Related to Figure 2

(A) Pull-down binding assays showing interactions between MBP-FUS wt or chimeras with GST-Kapβ2, GST-Impα/β, GST-Kap121 or GST-Crm1.

(B and C) Dissociation constants (K_Ds) measured at 20°C by ITC of Kapβ2 binding to MBP-FUS(453-526) (B) and MBP-FUS(371-526) (C). Thermograms, binding isotherms and data fit residuals of two independent ITC experiments are plotted. K_Ds, obtained from NITPIC (integration software that estimates baseline error from individual isotherm data points) and SEDPHAT (performs global fitting of independent ITC experiments), are reported with 68.3% confidence interval in brackets.

(D) Overall structure of Kapβ2 (pink) in complex with FUS(456-526) (green). Kicked omit map (cyan mesh) within 10 Å of all Kapβ2 residues, contoured at 3.0σ, is overlaid on the structure.

(E) Overall structure of Kapβ2 (pink) in complex with FUS(371-526) (green). Kicked omit map (cyan mesh) within 10 Å of all Kapβ2 residues, contoured at 3.0σ, is overlaid on the structure.

(F) Crystals of the Kapβ2•full length FUS complex were harvested, washed in crystallization reservoir solution, dissolved in buffer and visualized by Coomassie Blue-stained SDS/PAGE.

(G) Stereo-images of the 4Å resolution structure of Kapβ2 (pink cartoon) bound to full length FUS where only residues 508-526 of FUS are modeled (blue ribbon with side chain sticks). Kicked omit map (light gray mesh) within 10 Å of all Kapβ2 residues, contoured at 2.5σ and 2.0σ levels are shown. There are no obvious densities for extensive FUS interaction with Kapβ2 in addition to the NLS.

(H) Superimposed structures of FUS from four complexes: Kapβ2-FUS full-length (blue), Kapβ2•FUS(371-526) (yellow), Kapβ2•FUS(456-526) (green) and Kapβ2•FUS(498-526) (red; PDB: 4FDD).

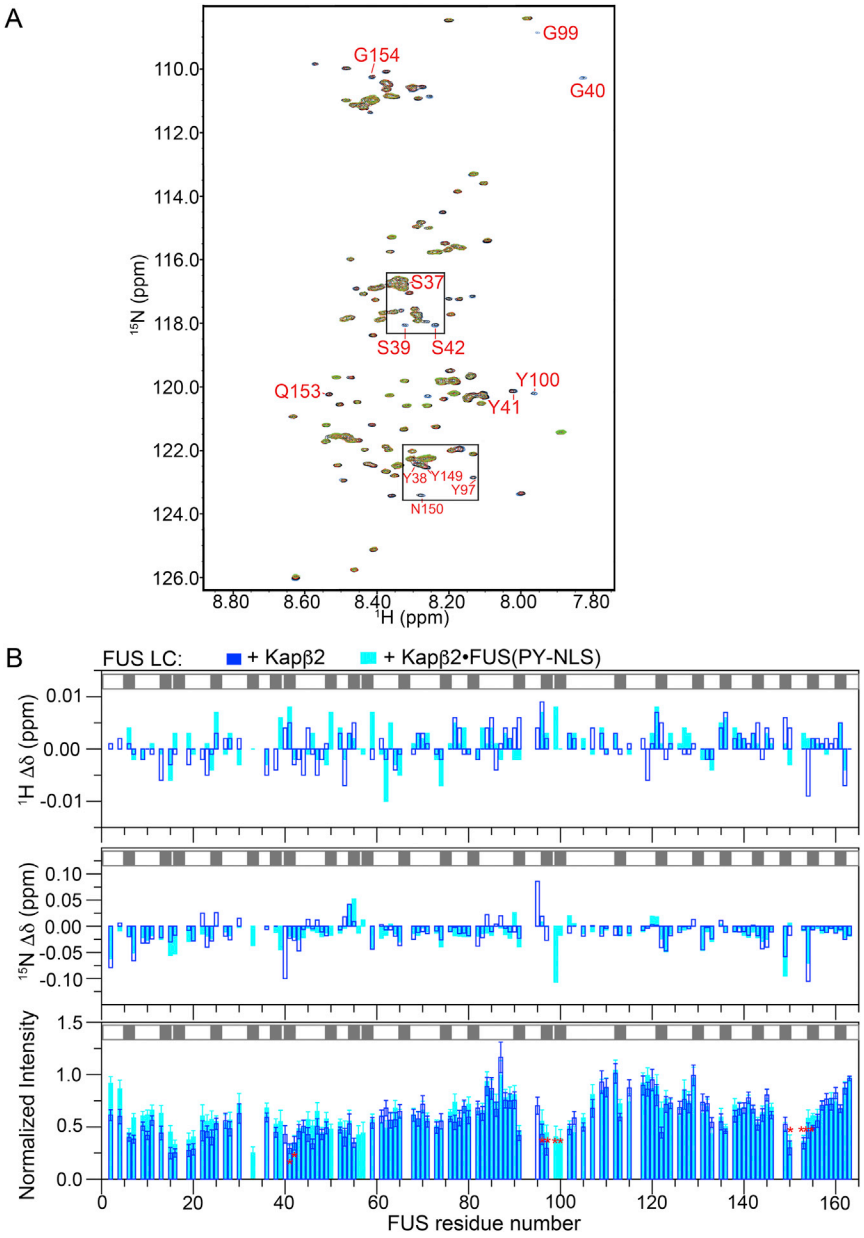

Figure S3. NMR Analyses Kapβ2 Binding to FUS LC, Related to Figure 3

(A) Overlay of 2D ^{1}H-^{15}N spectra of 75 μM ^{15}N-labeled FUS LC alone (blue) or with increasing concentrations of Kapβ2: 37.5 μM (0.5:1, black), 75 μM (1:1, red), 112.5 μM (1.5:1, green). Residues in several regions of FUS LC show chemical shifts and intensity attenuations (see Figure 5A) and three of the most affected regions are 37-41, 97-100, 149-154.

(B) NMR chemical shift deviations at 10°C of 75 μM FUS LC resonances in the presence of 100 μM Kapβ2 (dark blue open bars) or 100 μM Kapβ2•FUS PY-NLS complex (light blue) compared to 75 μM FUS LC alone. NMR chemical shift deviations, ^{1}H (top) and ^{15}N (middle), and resonance intensity attenuation (bottom) are plotted. ^{1}H and ^{15}N resonances show very similar changes upon addition of Kapβ2 alone or FUS PY-NLS-bound Kapβ2. Chemical shift differences of ^{1}H (top) and ^{15}N (middle) resonance position as well as resonance intensity attenuation (bottom) support FUS LC binding weakly to Kapβ2 across the entire FUS LC domain. Three segments ^{37}SYSGY^{41}, ^{97}YPGY^{100} and ^{149}YSPPSG^{154} (gray bars mark positions of the 24 tyrosines) show larger resonance intensity attenuation (red asterisks) and large ^{15}N and/or ^{1}H chemical shift differences, suggesting stronger Kapβ2-binding to those elements. Error bars in (B) represent errors propagated from the measurement of noise in the NMR spectra.

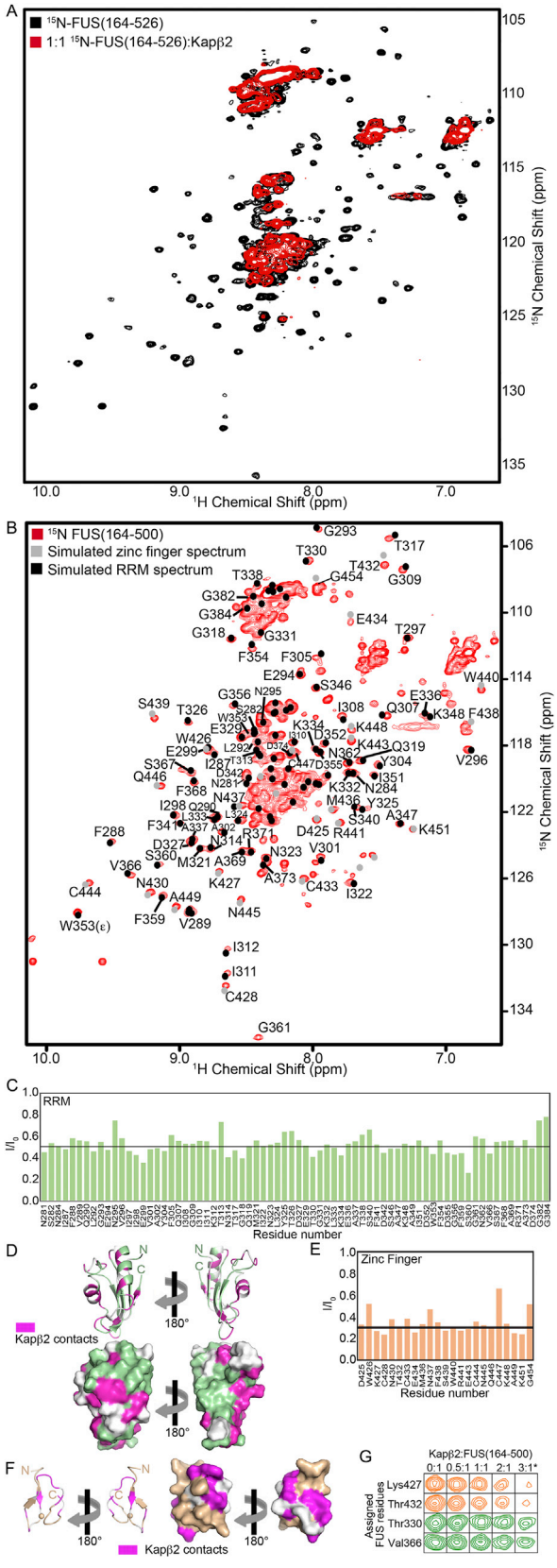

(legend on next page)

Figure S4. NMR Analyses of Kapβ2 Binding to RRM and ZnF Domains within FUS(164–500), Related to Figure 4

(A) Overlay of $^{1}H/^{15}N$ HSQC NMR spectrum of ^{15}N-FUS(164-526) alone (black) or with equimolar Kapβ2.

(B) Overlay of $^{1}H/^{15}N$ HSQC NMR spectrum of ^{15}N-FUS(164-500) with simulated spectra of the FUS RRM and zinc finger domains based on reported chemical shifts of the isolated domains (Liu et al., 2013; Iko et al., 2004).

(C) Attenuation of assigned RRM domain resonances in $^{1}H/^{15}N$ HSQC NMR spectra of ^{15}N-FUS(164-500) upon addition of 3-fold molar excess of Kapβ2•M9M (I = resonance intensity in the presence of Kapβ2•M9M; I_0 = resonance intensity of FUS alone).

(D) Ribbon (top) and surface representations (middle and bottom panels) of the FUS RRM (PDB: 1LCW, green), showing residues with $I/I_0 < 0.5$ upon binding Kapβ2 (magenta). Unassigned residues are white.

(E) Attenuation in intensity of assigned ZnF domain resonances in $^{1}H/^{15}N$ HSQC NMR spectra of ^{15}N-FUS(164-500) upon addition of 3-fold molar excess of Kapβ2•FUS PY-NLS.

(F) Ribbon and surface representations of the homology model of the FUS ZnF domain generated from structure of zinc finger in ZNF265, PDB: 2K1P, orange. Residues with $I/I_0 < 0.3$ upon Kapβ2 binding are in magenta and unassigned residues are white.

(G) Selected resonances from ZnF (orange) and RRM (green). Asterisk indicate Kapβ2•M9M complex. All other columns are Kapβ2•FUS PY-NLS.

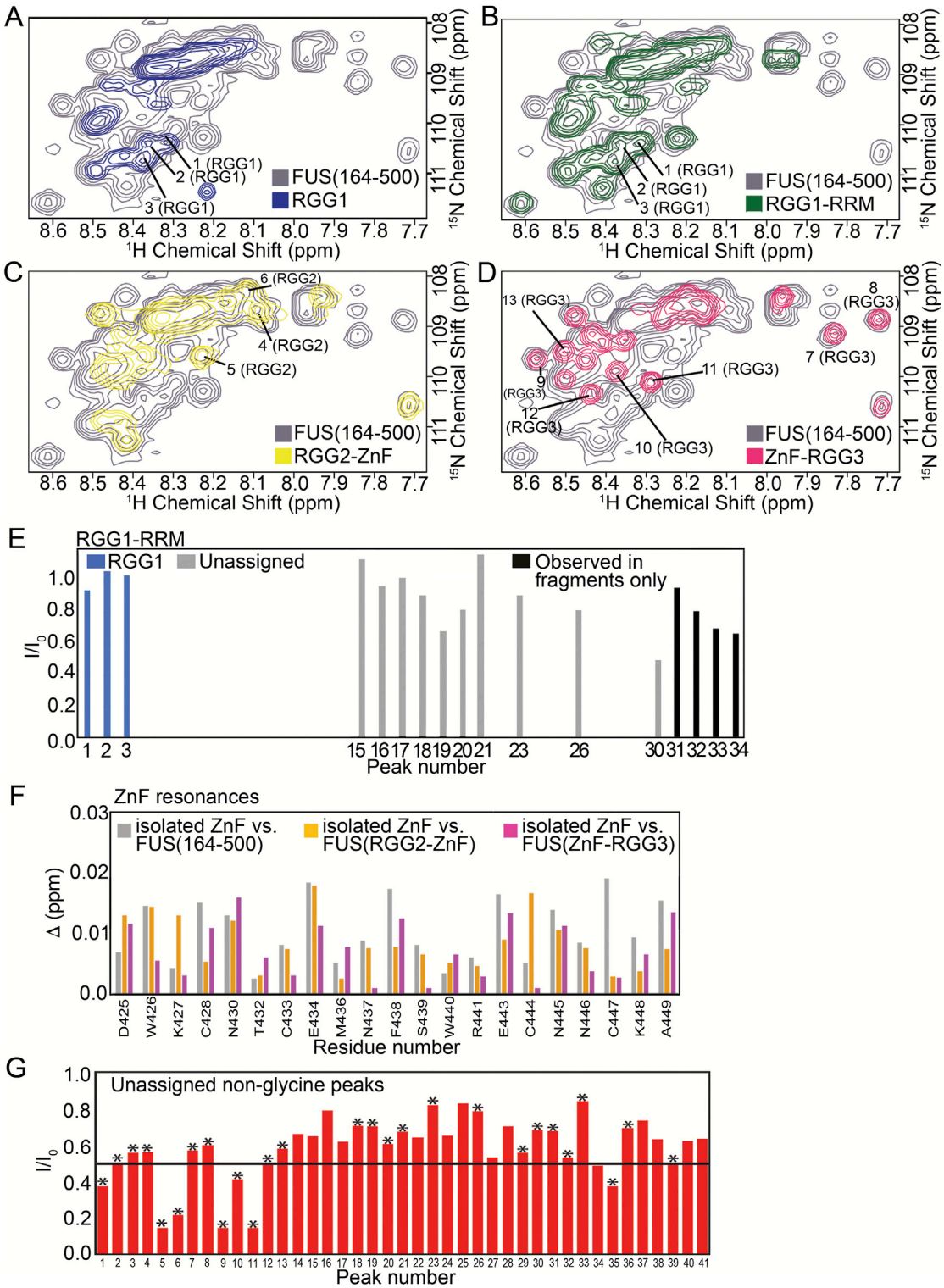

Figure S5. NMR Analyses of Kapβ2 Binding RGG1, RGG2, and RGG3 Regions of FUS(164-500), Related to Figure 5

(A–D) Glycine residues in FUS(164-500) were assigned to RGG1, RGG2 and RGG3 regions by overlaying ^{1}H/^{15}N spectra of FUS(164-500) and (A) RGG1 containing FUS residues 164-267, (B) RGG1-RRM containing FUS residues 164-370, (C) RGG2-ZnF containing FUS residues 371-452, (D) ZnF-RGG3 containing FUS residues 421-500. Glycine crosspeaks observed in spectra of only RGG1/RGG1-RRM or only RGG2 or only RGG3 could be assigned to that fragment, and are indicated in the spectra.

(legend continued on next page)

(E) Attenuation in intensity of glycine peaks in $^{1}H/^{15}N$ HSQC NMR spectra of ^{15}N-FUS(RGG1-RRM) upon addition of 2-fold molar excess of Kapβ2•M9M.
(F) Chemical shift differences, $\Delta = [(\Delta^{1}H)^{2} + ((0.1*\Delta^{15}N))^{2}]^{0.5}$, in ZnF resonances between the isolated domain (FUS residues 422-453), FUS(164-500) (gray bars), RGG2-ZnF (yellow bars) and ZnF-RGG3 (magenta bars). The ZnF chemical shifts were identical within experimental error in all constructs. Additionally, with the exception of only a few cross peaks likely at the termini of the constructs, the glycine chemical shifts of the RGG1, RGG2-ZnF and ZnF-RGG3 fragments were virtually exact subsets of those in FUS(164-500) (panels A-D). These data strongly suggest that the ZnF domain behaves independently in FUS(164-500) and does not make significant intramolecular contacts with surrounding regions. The similarity of chemical shifts across four different constructs indicates that if such intramolecular interactions are present, the self-interacting states must be populated to a small degree. Moreover, even in the case of multi-site exchange (involving for example all three RGG regions competing for a common site on the ZnF domain), where divergent chemical shifts might be averaged out, these differences should be revealed in spectra of the smaller fragments where competition for those sites would be eliminated. Yet the chemical shifts of all the fragments are identical within experimental error to each other and to those in FUS(164-500). Because of these data, we conclude that the ZnF makes few or no intramolecular contacts in FUS.
(G) Attenuation of unassigned non-glycine resonances (arbitrarily numbered; Table S2) in $^{1}H/^{15}N$ HSQC NMR spectra of ^{15}N-FUS(164-500) upon addition of 3-fold molar excess of Kapβ2•M9M. Asterisks indicate resonances not in RRM or zinc finger domains based on reported chemical shift assignments as in Figure S4A.

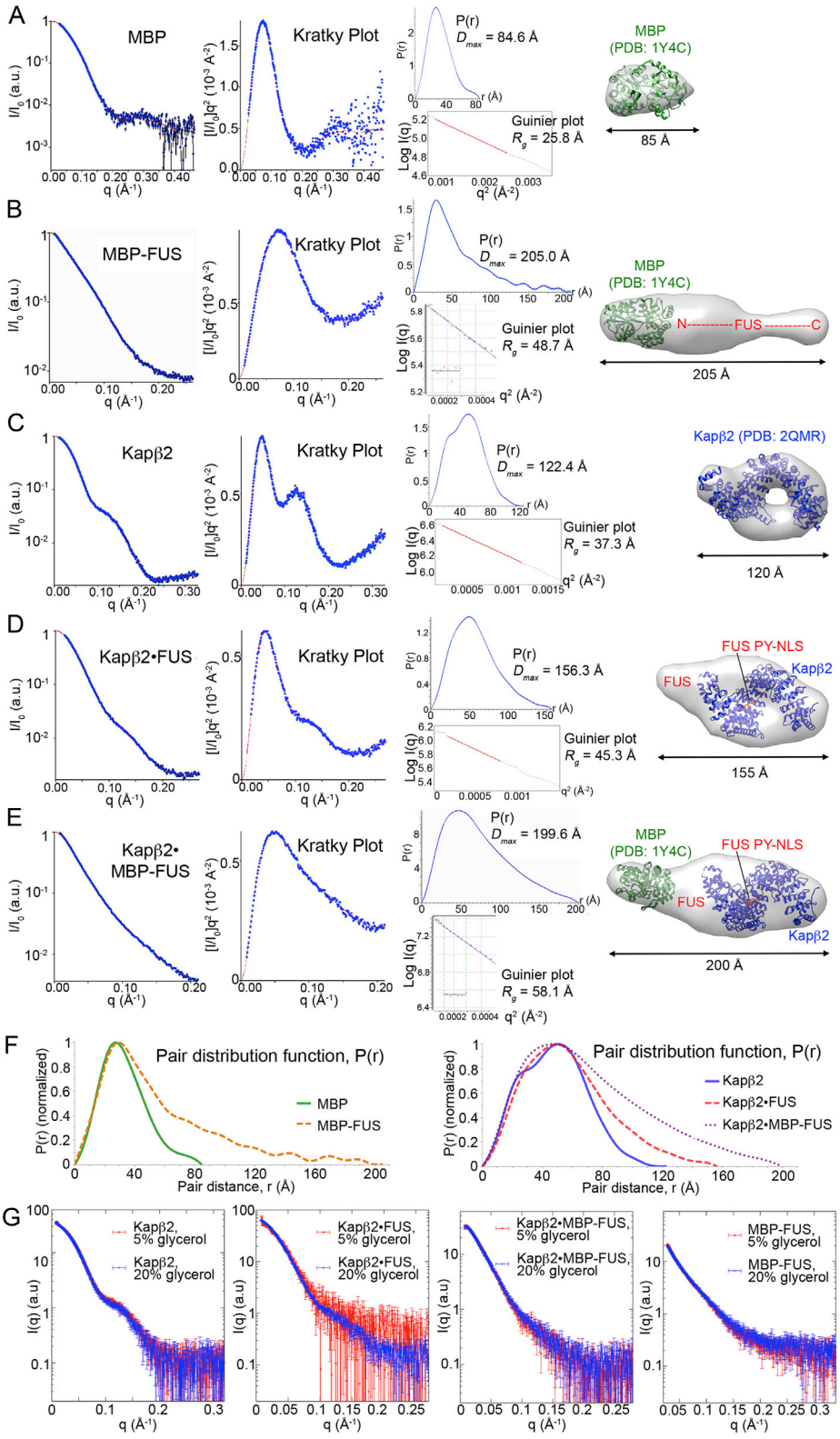

Figure S6. SAXS Analysis of MBP, MBP-FUS, Kapβ2, Kapβ2·FUS, and Kapβ2·MBP-FUS, Related to Figure 6A

(A–E) SAXS profiles of MBP (A), MBP-FUS (B), Kapβ2 (C), Kapβ2•FUS (D), and Kapβ2•MBP-FUS (E) were used to compute radius of gyration (R_g), maximum particle size (D_{max}), pair distribution function (P(r)), and *ab initio* shapes. (A–E, left panels) The experimental SAXS profile (blue dots with black error bars) is shown

(legend continued on next page)

along with the extrapolation curve (red). The corresponding Kratky plot (used to depict the level of flexibility) is also shown in blue dots along with the extrapolation curve (red). A high plateau in the Kratky plot (q = 0.15 - 0.2 $Å^{-1}$) suggests some flexibility in MBP-FUS (B). (A–E, middle panels) The top plot shows the pair distribution function, P(r). The maximum particle size (*Dmax*) was determined as the maximum pair distance in the plot. The bottom plot shows the corresponding Guinier plot with the calculated R_g fit value in A. The linearity of the Guinier plots confirms a high degree of homogeneity for each of the five SAXS samples. (A–E, right panels) A view of the *ab initio* shape (represented as a transparent envelope) computed from the experimental SAXS profile. Structures of MBP (PDB: 1Y4C), Kapβ2 (PDB: 2QMR), and FUS PY-NLS of full length FUS (Figures S2F and S2G) were coarsely fitted to the SAXS envelopes.

(F) Comparison of the pair distribution functions, P(r) between MBP (green curves) and MBP-FUS (orange dots), and among Kapβ2 (blue curves), Kapβ2•FUS (red dots), and Kapβ2•MBP-FUS (purple dots). MBP-FUS is significantly extended compared to MBP. In contrast, FUS becomes more compact upon binding Kapβ2.

(G) Comparison of the SAXS profiles (at ~1.0 mg/mL) of Kapβ2, Kapβ2•FUS, Kapβ2•MBP-FUS, and MBP-FUS collected in 5% (red curves) and 20% (blue curves) glycerol buffers, respectively. SAXS profiles of the same proteins are nearly identical within their uncertainties, regardless of the glycerol concentration. Therefore, glycerol concentrations from 5 to 20% do not affect protein compaction. Note that Kapβ2•FUS in 5% glycerol was prepared at a low concentration of ~0.5 mg/mL, leading to the high standard deviation in its SAXS profile.

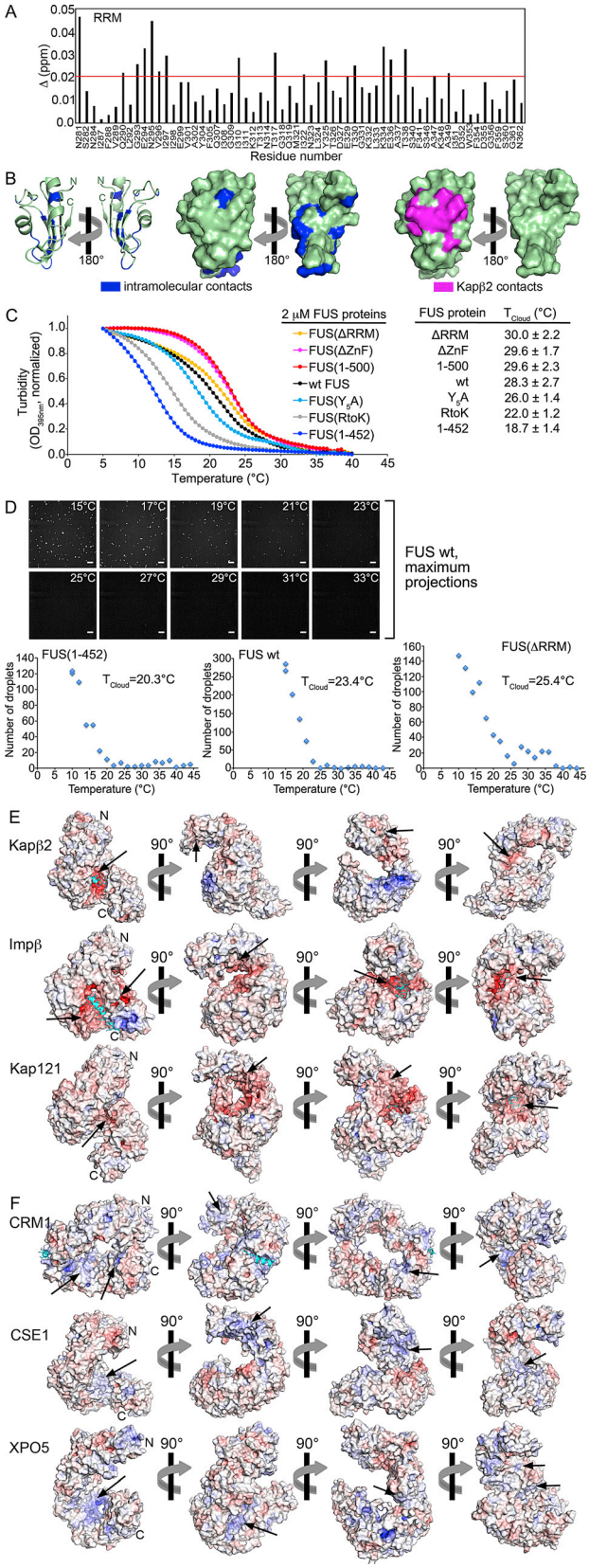

(legend on next page)

Figure S7. RRM Participates in Intramolecular Interactions within FUS(164-500), Temperature Dependence of FUS Phase Separation, and Electrostatic Surfaces of Karyopherin Proteins, Related to Figure 7 and Discussion

(A) Chemical shift differences, $\Delta = [(\Delta^{1}H)^{2} + ((0.1*\Delta^{15}N))^{2}]^{0.5}$, between the isolated RRM (FUS residues 285-371) and the RRM within FUS(164-500).

(B) Ribbon and surface representations of the FUS RRM (PDB: 1LCW, green), with residues $\Delta > 0.02$ colored blue. Residues that directly contact Kapβ2 based on cross saturation transfer data are colored magenta (Figure 4B). At 2 μM and 8 μM concentration, FUS(ΔRRM) has a higher T_{cloud} than wild-type FUS, indicating that deletion of the RRM favors phase separation. To gain insight into this behavior, we compared the chemical shifts of the isolated RRM domain to those of the RRM within FUS(164-500). A number of amide resonances, mostly on the face of the domain opposite the Kapβ2 binding site, differ between the two constructs. This observation suggests that in FUS(164-500), RRM participates in intramolecular contacts with the RGG regions, which could sequester these elements. Given that the RGG regions play important roles in phase separation, their sequestration by RRM may suppress phase separation.

(C) Temperature dependence of FUS phase separation. Turbidity (OD_{395nm}) of 2 μM MBP-FUS proteins (wild-type (WT) and mutants) after 3 h treatment with Tev protease was monitored as temperature was decreased from 40°C or 45°C to 5°C. Optical densities were normalized to values measured at 5°C. T_{Cloud} is the x-intercept of the tangent at the inflection point of the curve (mean of 3 technical replicates, ± SD).

(D) Mixtures containing 2 μM MBP-FUS WT, MBP-FUS(1-452), or MBP-FUS(ΔRRM), 20 nM FUS-GFP were treated with Tev protease at room temperature for 50 min to form FUS droplets. The phase separated mixtures were cooled to either 10°C or 15°C, held at those temperatures for 2 min, and then increased by 2°C increments to a maximum temperature of 43°C or 44°C. The sample was held at each temperature for 2-3 min prior to acquisition of a 50 μm Z stack (1 μm increments) using spinning disk confocal microscopy. Panels show maximum projection images derived from the Z stack 10-50 μm above the slide surface. To calculate T_{cloud}, images in this same portion of the Z stack were segmented using the Triangle algorithm in ImageJ and the total number of FUS droplets was determined after a filter for circularity (> 0.5) and size (> 0.5 μm^2). T_{cloud} was determined from the x-intercept of a line fit to the first six (WT and FUS(1-452)) or eight (FUS(ΔRRM)) points in the (number of puncta) versus temperature curve.

(E) Electrostatic surface potential (scale of -12 kTe^{-1} to $+12$ kTe^{-1}) of importins Kapβ2 (PDB: 4FDD), Impβ (1QGK) and Kap121 (3W3W). PY-NLS bound to Kapβ2, IBB (NLS) bound to Impβ and IK-NLS bound to Kap121 are shown as cyan cartoons. Arrows point to acidic patches on the concave surface of the importins.

(F) Electrostatic surface potential (scale of -12 kTe^{-1} to $+12$ kTe^{-1}) of Exportins CRM1 (PDB: 3GB8), CSE1 (1WA5) and XPO5 (3A6P). The NES (residues 1-15) of cargo SNUPN bound to CRM1 is shown as a cyan cartoon. Cargos bound to CSE1 (Impα) and XPO5 (pre-miRNA), along with bound RanGTP, were removed to allow viewing of the concave surfaces of the Exportin. Arrows point to basic patches on the concave surface of the Exportins.